Received: 2 June 2022 | Revised: 30 September 2022 | Accepted: 4 October 2022

DOI: 10.1002/nme.7166

RESEARCH ARTICLE

WILEY

Hourglassing- and locking-free mesh distortion insensitive Petrov–Galerkin EAS element for large deformation solid mechanics

Robin Pfefferkorn | **Peter Betsch**

Institute of Mechanics, Karlsruhe Institute of Technology (KIT), Karlsruhe, Germany

Correspondence
Peter Betsch, Institute of Mechanics, Karlsruhe Institute of Technology (KIT), 76131 Karlsruhe, Germany.
Email: peter.betsch@kit.edu

Funding information
Deutsche Forschungsgemeinschaft, Grant/Award Number: 466086399

Abstract

We present a novel geometrically nonlinear EAS element with several desirable features. First, a Petrov–Galerkin ansatz significantly improves the element's performance in distorted meshes without loosing the simple strain-driven format. Second, the recently proposed mixed integration point strategy is employed to improve the element's robustness in the Newton–Raphson scheme. Finally and most importantly, we enhance the spatial displacement gradient instead of the usually modified deformation gradient. This allows to construct an element without the well-known spurious instabilities in compression and tension as shown numerically and supported by a corresponding hypothesis. All in all, this leads to a robust, stable, locking-free, and mesh distortion insensitive finite element successfully applied in a wide range of examples.

KEYWORDS

enhanced assumed strain (EAS), hourglassing instabilities, mixed finite elements, mixed integration point, Petrov–Galerkin, unsymmetric finite element method

1 | INTRODUCTION

Countless mixed finite elements have been developed throughout the last 50 years with the goal to cure *locking* and other defects of low-order finite elements. One of the probably most successful element groups are *enhanced assumed strain* (EAS) elements due to their simplicity and strain driven format which allows straightforward implementation of complex material models. The EAS framework has first been proposed in the early 1990s by Simo and Rifai[1] and Simo and Armero[2] for linear and nonlinear problems, respectively, and is a mathematically sound successor of the earlier proposed incompatible mode models.[3,4] Since then, the EAS method has been implemented into several commercial codes and has not only been successfully applied in solid mechanics[2,5-19] but also to model shell structures, diffusion problems and even fracture problems.[20-25] Despite the tremendous effort put in development of EAS elements there are still some open issues. Pfefferkorn and Betsch[26] discuss three of which: robustness in the Newton–Raphson scheme, mesh-distortion sensitivity and hourglassing instabilities. All three are addressed in this contribution.

The first issue concerns *robustness* in the Newton–Raphson scheme by which we herein denote two properties: maximum size of applicable load steps and number of Newton–Raphson iterations required for convergence.[19] In this regard assumed stress elements are by far superior to both displacement-based elements[27,28] and EAS elements.[19,29] To improve robustness of displacement based elements Magisano et al.[30] recently proposed the *mixed integration point* (MIP) method

in the context of shell problems. It allows to substantially increase the robustness by a simple modification which only affects the finite element tangent without changing the residual (and therefore the solution). This approach has recently been extended to EAS elements[19] and is also employed in the present contribution in order to improve robustness of the Petrov–Galerkin EAS approach at hand.

Regarding the second issue, *mesh distortion sensitivity*, there exists a fundamental publication by MacNeal[31] (see also the preliminary work[32]) which has in the opinion of the authors not gotten the attention it deserves. In that work MacNeal[31] *proves* (see also Pfefferkorn and Betsch[18]) that a finite element for linear elasticity with symmetric stiffness matrix *cannot* simultaneously satisfy the patch test and be exact for higher order modes for arbitrary meshes. This ultimately leads to mesh distortion sensitivity of elements with symmetric stiffness matrices. However, MacNeal's theorem leaves a "loop-hole". Elements with an unsymmetric stiffness matrix can simultaneously pass the patch test and be mesh distortion insensitive. Constructing such finite elements is the key idea of the *unsymmetric finite element method* first proposed by Rajendran and Liew[33] for higher order elements (see also References[34-36]). That method is based on a *Petrov–Galerkin* approach instead of the usual *Bubnov–Galerkin* ansatz. Essentially, the trial functions of the displacements (actual field) are approximated with so-called *metric shape functions*[37] (constructed in the physical domain) while the test functions of the displacement (virtual field) are approximated as usual with parametric shape functions. This approach ultimately allows to greatly reduce the mesh distortion sensitivity.

A major drawback of all unsymmetric finite elements is of course the increased computational cost. This concerns especially the factorization of the non-symmetric stiffness matrix. The time required for that step is compared to standard elements in the work.[18] However, the additional effort is, in the opinion of the authors, more than compensated by the increased coarse mesh accuracy and the reduced mesh distortion sensitivity.

Unfortunately, it is not as straightforward to construct unsymmetric low-order finite elements because a careful choice of ansatz functions is required for optimal performance.[18,38] This led previously to methods with complex ansatz functions that depend on the material model[36,38-42] or that require higher order numerical integration.[43] Unsymmetric finite element approaches without these drawbacks have recently been published by Pfefferkorn and Betsch[18] in the form of a *Petrov–Galerkin EAS* (PG-EAS) framework and by Huang et al.[44] on the basis of an incompatible mode approach. Both elements are developed for linear elasticity and maintain the substantially decreased mesh distortion sensitivity of the unsymmetric finite element method. Moreover, the approach by Pfefferkorn and Betsch[18] is completely locking-free, enables exact integration of the finite element integrals with standard Gauss quadrature and reduces to the standard EAS method in case of regular meshes. In this work we straightforwardly apply the unsymmetric PG-EAS approach by Pfefferkorn and Betsch[18] to nonlinear problems and show that it has similar beneficial effects. Mesh distortion sensitivity is greatly reduced even though it is not possible to get analytic results as in the linear elastic case. Furthermore, we propose a modification of the three volumetric modes required in 3D for a completely locking free element.[18] This adjustment allows to skip the computationally expensive Gram–Schmidt orthogonalization required in aforementioned reference and is motivated by higher-order analytic solutions of linear elasticity similar to the ones given by Nadler and Rubin.[45]

The final and probably most important open issue of EAS elements concerns spurious *hourglassing instabilities*. This issue was already mentioned in the conclusion of the seminal work on geometrically nonlinear EAS elements by Simo and Armero[2] and has first been thoroughly discussed by Wriggers and Reese[46] for hyperelasticity and by de Souza Neto et al.[47] for elasto-plasticity. One of the most successful attempts to remove the instability has been proposed by Korelc and Wriggers[7] (see also Glaser and Armero[10,48], who adopted the element for frame invariance). They established that using the *transpose* of the originally employed *Wilson-modes* for the enhanced field removes the instability under compression. Unfortunately though, this attempt could not cure hourglassing under tension. Other methods to suppress the spurious behavior use artificial hourglass stabilization with user-defined parameters,[10,48,49] hourglass stabilization based on mixed methods[50-52] or combine the EAS method with other mixed elements.[53-59] However, none of these alternative approaches led to the desired result of a completely stable, locking-free element without artificial stabilization. A final avenue followed to overcome the hourglassing issue is enhancing different kinematic fields than the originally[2] proposed and most frequently employed enhancement of the deformation gradient (F-enhancement). Unfortunately, both enhancement of the Green–Lagrange strain (E-Enhancement)[11,21,48,51,60-62], which is often employed in shell-structures, and enhancement of the right stretch tensor (U-enhancement)[6,48,63] do not lead to entirely stable formulations.

In the present contribution we add another kinematic field to the list of enhanced fields: the spatial displacement gradient (h-enhancement) as suggested by Schmied[64] (PhD-thesis, only available in German). This allows to finally overcome the issue of hourglassing-instabilities of EAS elements both in tension and compression without loosing other favorable properties. On top of that, we establish a hypothesis on why h-enhancement is much more stable. It is closely related to the ad-hoc formulated volume-condition proposed by Nagtegaal and Fox[65] which is justified in this work. Essentially, we

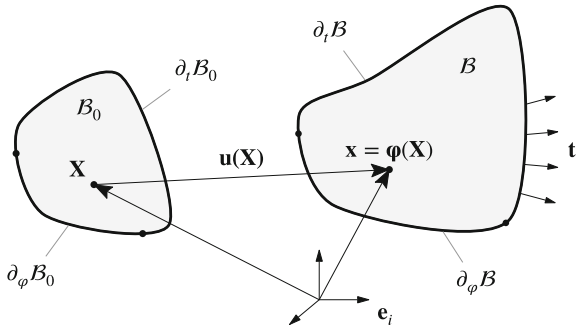

FIGURE 1 Configurations and kinematics of a deformable body $\mathcal{B}$.

suggest that the instabilities of previously developed EAS elements are linked to the well-known checkerboard modes observed for mixed pressure elements through the eliminated stress field.

In summary, this work introduces a novel PG-EAS element based on h-enhancement which overcomes some of the most serious issues of existing EAS elements. The presentation starts with essential continuum mechanics and the weak form in Section 2. The approximations of the various fields with the finite element method are covered in Section 3 where focus is put on the Petrov–Galerkin formulation and the required metric shape functions. Analytic solutions of higher-order linear elasticity are given in Appendix A and used for the new volumetric enhanced modes in Section 3.2. Section 4 covers analytic proofs that the element on the one hand meets basic requirements and on the other hand has interesting features explaining its outstanding performance. The decreased mesh-distortion sensitivity and the increased numerical stability are discussed in Sections 4.5 and 4.9, respectively. Finally, in-depth elastic and elasto-plastic numerical investigations covering a wide range of benchmarks are described in Section 5 before conclusions are drawn in Section 6.

2 | WEAK FORM

This section covers fundamental continuum mechanic relations in Section 2.1 and introduces the key idea of the novel EAS framework in Section 2.2. With these basics at hand we then introduce in Section 2.3 the weak form for the new class of EAS elements.

2.1 | Continuum mechanics

We consider as usual the deformation of a body from its reference configuration $\mathcal{B}_0 \in \mathbb{R}^3$ to a spatial configuration $\mathcal{B} \in \mathbb{R}^3$ (see Figure 1).

In this process material points $\mathbf{X} \in \mathcal{B}_0$ are mapped to corresponding spatial points $\mathbf{x} = \boldsymbol{\varphi}(\mathbf{X}) \in \mathcal{B}$ by the bijective *deformation map*

$$\boldsymbol{\varphi} \in \mathcal{U} = \left\{ \boldsymbol{\varphi} : \mathcal{B}_0 \to \mathbb{R}^3 \,\middle|\, (\boldsymbol{\varphi})_i \in \mathrm{H}_1, \quad \det(\mathrm{D}\boldsymbol{\varphi}) > 0, \quad \boldsymbol{\varphi}(\mathbf{X}) = \overline{\boldsymbol{\varphi}}(\mathbf{X}), \mathbf{X} \in \partial_\varphi\mathcal{B}_0 \right\}. \tag{1}$$

Therein, H_1 denotes a Sobolev space and $\partial_\varphi\mathcal{B}_0 \subseteq \partial\mathcal{B}_0$ is a part of the body's boundary $\partial\mathcal{B}_0$ on which the deformation is prescribed by $\overline{\boldsymbol{\varphi}}(\mathbf{X})$. On the remaining part of the boundary $\partial_t\mathcal{B}_0 = \partial\mathcal{B}_0 \setminus \partial_\varphi\mathcal{B}_0$ boundary conditions are prescribed in the form of given traction $\mathbf{t}$. Linearization of the deformation map $\boldsymbol{\varphi}$ with respect to the coordinates $\mathbf{X}$ determines the *deformation gradient*[*]

$$\mathbf{F}_\varphi = \frac{\partial \boldsymbol{\varphi}}{\partial \mathbf{X}} = \nabla_{\mathbf{X}} \boldsymbol{\varphi}, \tag{2}$$

where we use index $(\bullet)_\varphi$ to emphasize that the field $(\bullet)$ depends solely on the deformations (this will not necessarily be the case in subsequent sections). Furthermore,

$$\mathbf{u}(\mathbf{X}) = \boldsymbol{\varphi}(\mathbf{X}) - \mathbf{X} \tag{3}$$

is the displacement of a material point $\mathbf{X}$. Taking the derivative of $\mathbf{u}$ with respect to $\mathbf{X}$ and $\mathbf{x}$ yields the material and spatial *displacement gradient* given by

$$\mathbf{H}_\varphi = \frac{\partial \mathbf{u}}{\partial \mathbf{X}} = \nabla_{\mathbf{X}} \mathbf{u} = \mathbf{F}_\varphi - \mathbf{I}, \tag{4a}$$

$$\mathbf{h}_\varphi = \frac{\partial \mathbf{u}}{\partial \mathbf{x}} = \nabla_{\mathbf{x}} \mathbf{u} = \mathbf{I} - \mathbf{F}_\varphi^{-1}, \tag{4b}$$

respectively. The link of the displacement gradients to the deformation gradient given in (4) can easily be established via (2) and (3). Moreover, in view of (4), it is straightforward to establish the relations

$$\mathbf{h} = \mathbf{H}\mathbf{F}^{-1}, \qquad \mathbf{F} = (\mathbf{I} - \mathbf{h})^{-1}, \tag{5}$$

frequently used for the present EAS element. We omit index φ in the last equation and subsequently whenever a relation can and will also be used for general and not only purely deformation based fields.

In addition to the kinematic relations presented above, a constitutive law is required to model different material behavior. A broad class of material models can be written in terms of the *Kirchhoff stress* as

$$\hat{\boldsymbol{\tau}} = \hat{\boldsymbol{\tau}}(\mathbf{F}, \boldsymbol{\Xi}), \tag{6}$$

where $\boldsymbol{\Xi}$ denotes the internal variables necessary to describe inelastic behavior. The usual transformation rules

$$\hat{\boldsymbol{\tau}} = \hat{\mathbf{P}}\mathbf{F}^{\mathrm{T}} = \mathbf{F}\hat{\mathbf{S}}\mathbf{F}^{\mathrm{T}} \tag{7}$$

relate the constitutive Kirchhoff stress $\hat{\boldsymbol{\tau}}$ to the corresponding *first* and *second Piola-Kirchoff stress* tensors denoted by $\hat{\mathbf{P}} = \hat{\mathbf{P}}(\mathbf{F}, \boldsymbol{\Xi})$ and $\hat{\mathbf{S}} = \hat{\mathbf{S}}(\mathbf{F}, \boldsymbol{\Xi})$, respectively.

Remark 1. For a homogeneous hyperelastic material model (6) is fully defined by a strain energy function W and given by

$$\hat{\boldsymbol{\tau}} = \frac{\partial W}{\partial \mathbf{F}}\mathbf{F}^{\mathrm{T}} = 2\mathbf{F}\frac{\partial W}{\partial \mathbf{C}}\mathbf{F}^{\mathrm{T}}, \tag{8}$$

where $\mathbf{C} = \mathbf{F}^{\mathrm{T}}\mathbf{F}$ is the right Cauchy-Green tensor.

2.2 | EAS kinematics

The key idea of the EAS method is to *enhance* a kinematic field with an *incompatible part*. This was first proposed for geometrically nonlinear problems by Simo and Armero[2] who recast the total deformation gradient $\mathbf{F}$ in the form (F-enhancement)

$$\mathbf{F}(\boldsymbol{\varphi}, \boldsymbol{\alpha}) = \mathbf{F}_\varphi(\boldsymbol{\varphi}) + \tilde{\mathbf{F}}(\boldsymbol{\varphi}, \boldsymbol{\alpha}). \tag{9}$$

Thus, the compatible (purely deformation dependent) deformation gradient $\mathbf{F}_\varphi$ (2) is enhanced with the incompatible part $\tilde{\mathbf{F}}$ which contains the additional degrees of freedom $\boldsymbol{\alpha}$. However, as mentioned in the introduction, it is also possible to enhance various other kinematic fields. In the present work we choose to enhance the spatial displacement gradient (4b) in the same way as (9) such that (h-enhancement)

$$\boxed{\mathbf{h}(\boldsymbol{\varphi}, \boldsymbol{\alpha}) = \mathbf{h}_\varphi(\boldsymbol{\varphi}) + \tilde{\mathbf{h}}(\boldsymbol{\varphi}, \boldsymbol{\alpha}),} \tag{10}$$

where now instead of $\tilde{\mathbf{F}}$ in (9) the *enhanced spatial displacement gradient* $\tilde{\mathbf{h}}$ is the independent field. Note that the total deformation gradient now results from

$$\mathbf{F}(\boldsymbol{\varphi}, \boldsymbol{\alpha}) = (\mathbf{I} - \mathbf{h}(\boldsymbol{\varphi}, \boldsymbol{\alpha}))^{-1}, \tag{11}$$

which is in analogy to $(5)_2$. This idea of enhancing the spatial displacement gradient has to the best knowledge of the authors only been considered in the PhD-thesis by Schmied,[64] which is written in German. In that work it is shown

numerically that (10) can be used to construct elements without spurious hourglassing in explicit dynamic simulations. In the present contribution we use (10) in implicit static problems in order to obtain an hourglassing-free EAS element in both large strain elasticity and elasto-plasticity. Furthermore, we establish a hypothesis why h-enhancement is favorable in terms of stability (see Section 4.9).

2.3 | Weak form

2.3.1 | Continuous weak form

With the basic continuum mechanic relations at hand we now introduce the weak form of the governing equations for an element based on h-enhancement (10). It is given by: Find the deformation $\boldsymbol{\varphi} \in \mathcal{U}$, incompatible displacement gradient $\tilde{\mathbf{h}} \in \mathcal{F} = L_2$ and independent stress tensor $\boldsymbol{\tau} \in \mathcal{T} = L_2$ such that

$$\int_{\mathcal{B}_0} \tilde{\nabla}^{\mathrm{s}}_{\mathbf{x}} \delta\boldsymbol{\varphi} \,:\, \hat{\boldsymbol{\tau}} \mathrm{d}V + G_{\mathrm{ext}}(\delta\boldsymbol{\varphi}) = 0, \tag{12a}$$

$$\int_{\mathcal{B}_0} \delta\tilde{\mathbf{h}} \,:\, (\hat{\boldsymbol{\tau}} - \boldsymbol{\tau})\, \mathrm{d}V = 0, \tag{12b}$$

$$\int_{\mathcal{B}_0} \delta\boldsymbol{\tau} \,:\, \tilde{\mathbf{h}} \mathrm{d}V = 0, \tag{12c}$$

is satisfied for arbitrary test functions $\delta\boldsymbol{\varphi} \in \mathcal{V} = \{\boldsymbol{\varphi} : \mathcal{B}_0 \to \mathbb{R}^3 | (\boldsymbol{\varphi})_i \in \mathrm{H}_1, \boldsymbol{\varphi}(\mathbf{X}) = \mathbf{0}, \mathbf{X} \in \partial_\varphi \mathcal{B}_0\}$, $\delta\tilde{\mathbf{h}} \in \mathcal{E} = L_2$ and $\delta\boldsymbol{\tau} \in \mathcal{S} = L_2$. Here, $\delta(\bullet)$ is used for test functions and does not denote variations since (12) can in general not be derived from a variational functional[†]. Moreover, $\hat{\boldsymbol{\tau}}$ is the constitutive Kirchoff stress (6) evaluated with $\mathbf{F}$ defined via (11) and (10). The gradient $\tilde{\nabla}^{\mathrm{s}}_{\mathbf{x}}(\bullet)$ is the symmetric part of the spatial gradient

$$\tilde{\nabla}_{\mathbf{x}}(\bullet) = \nabla_{\mathbf{X}}(\bullet)\mathbf{F}^{-1}_{\varphi}, \tag{13}$$

which is closely related to $(5)_1$. Finally, the integrals in (12) are named internal parts of the weak form and $G_{\mathrm{ext}}(\delta\boldsymbol{\varphi})$ contains the contributions of the prescribed external body forces $\mathbf{b}$ and surface loads $\mathbf{t}$.

Remark 2. It is important to note that, unless the test function $\delta\tilde{\mathbf{h}}$ has the form $\delta\tilde{\mathbf{h}} = \delta\tilde{\mathbf{H}}\mathbf{F}^{-1}$, $\delta\tilde{\mathbf{H}} \in L_2$ in analogy to $(5)_1$, the weak form (12) leads in general to an unsymmetric stiffness matrix even without the Petrov–Galerkin approach introduced in Section 3.[64] Unfortunately, choosing $\delta\tilde{\mathbf{h}} = \delta\tilde{\mathbf{H}}\mathbf{F}^{-1}$ results in an element which exhibits spurious instabilities. However, the stiffness matrix is already unsymmetric due to the Petrov–Galerkin approach in Section 3 such that the unsymmetry imposed by the weak form is not a major issue.

Remark 3. The proposed weak form (12) is by far not the only possibility to develop an EAS framework. For example, the standard weak form for nonlinear EAS elements with F-enhancement (9) (e.g., References[2,10,16]) is given by

$$\int_{\mathcal{B}_0} \nabla_{\mathbf{X}} \delta\boldsymbol{\varphi} \,:\, \hat{\mathbf{P}} \mathrm{d}V + G_{\mathrm{ext}}(\delta\boldsymbol{\varphi}) = 0, \tag{14a}$$

$$\int_{\mathcal{B}_0} \delta\tilde{\mathbf{F}} \,:\, (\hat{\mathbf{P}} - \mathbf{P}) \mathrm{d}V = 0, \tag{14b}$$

$$\int_{\mathcal{B}_0} \delta\mathbf{P} \,:\, \tilde{\mathbf{F}} \mathrm{d}V = 0. \tag{14c}$$

A similar formulation based on enhancement of the Green–Lagrange strains (E-enhancement) is also possible (e.g., References [11,21,48,51,66]). The crucial advantage of the weak form (12) based on $\mathbf{h}$ is that it allows the construction of elements without spurious instabilities. Thus, (12) is mainly considered in the sequel. Nevertheless, we also cover elements based on (14) for comparison with the novel displacement gradient enhanced elements.

2.3.2 | Discrete weak form

One particularity of EAS elements regarding the weak form is the assumption of L_2-orthogonal discrete[‡] test and trial spaces for the independent stress $\boldsymbol{\tau}^{\mathrm{h}}$ and incompatible strain $\tilde{\mathbf{h}}^{\mathrm{h}}$ (see References 1,2 and Section 4.7). In that way the independent stress field $\boldsymbol{\tau}^{\mathrm{h}}$ can be completely eliminated from (12) and the only remaining unknowns are $\boldsymbol{\varphi} \in \mathcal{U}^{\mathrm{h}}$ and $\tilde{\mathbf{h}}^{\mathrm{h}} \in \mathcal{E}^{\mathrm{h}}$. The discrete version of the weak form (12) is then given by

$$\boxed{\begin{aligned} G^{\mathrm{h}}_{\varphi} &= \int_{\mathcal{B}^{\mathrm{h}}_0} \tilde{\nabla}^{\mathrm{s}}_{\mathbf{x}} \delta\boldsymbol{\varphi}^{\mathrm{h}} \,:\, \hat{\boldsymbol{\tau}}^{\mathrm{h}} \mathrm{d}V + G^{\mathrm{h}}_{\mathrm{ext}}(\delta\boldsymbol{\varphi}^{\mathrm{h}}) = 0 \qquad \forall\, \delta\boldsymbol{\varphi}^{\mathrm{h}} \in \mathcal{V}^{\mathrm{h}}, \qquad (15a)\\ G^{\mathrm{h}}_{\alpha} &= \int_{\mathcal{B}^{\mathrm{h}}_0} \delta\tilde{\mathbf{h}}^{\mathrm{h}} \,:\, \hat{\boldsymbol{\tau}}^{\mathrm{h}} \mathrm{d}V = 0 \qquad \forall\, \delta\tilde{\mathbf{h}}^{\mathrm{h}} \in \mathcal{F}^{\mathrm{h}}, \qquad (15b) \end{aligned}}$$

where $\mathcal{U}^{\mathrm{h}}$, $\mathcal{V}^{\mathrm{h}}$, $\mathcal{E}^{\mathrm{h}}$, and $\mathcal{F}^{\mathrm{h}}$ are the discrete ansatz spaces for the various fields which are specified in Section 3.2.

3 | FINITE ELEMENT APPROXIMATION

We use very similar ansatz spaces for the present finite element as proposed by Pfefferkorn and Betsch[18] for a linear *Petrov–Galerkin* EAS (PG-EAS) element. These ansatz spaces are based on three design conditions determined in aforementioned reference and allow the construction of relatively simple, widely applicable, low-order, unsymmetric elements with exceptionally high accuracy in case of distorted meshes. However, the present nonlinear framework requires a few modifications to ensure objectivity and account for the nonlinear kinematics. In this section, we focus on these specifics and only briefly summarize the ansatz functions discussed at length by Pfefferkorn and Betsch.[18] Focus is put on three-dimensional (3D) *hexahedral elements* which can easily be reduced to two-dimensional (2D) quadrilaterals.

Moreover, we propose an improved version of the higher order enhanced modes required for 3D problems. A minor modification based on analytic solutions for linear elasticity given in Appendix A circumvents the need for the computationally expensive and intricate orthogonalization procedure originally employed in the work.[18]

3.1 | Geometry and skew coordinate frame

The reference geometry $\mathbf{X}^{\mathrm{h},e}$ of a hexahedral finite element Ω^e_0 with nodes $\mathbf{X}^e_i$, $i = 1, \dots, 8$ is described as usual with the *isoparametric* map such that the geometry map and the corresponding *Jacobian* are given by

$$\mathbf{X}^{\mathrm{h},e}(\boldsymbol{\xi}) = \sum_{i=1}^{8} N_i(\boldsymbol{\xi}) \mathbf{X}^e_i, \qquad \mathbf{J}^{\mathrm{h},e}(\boldsymbol{\xi}) = \frac{\partial \mathbf{X}^{\mathrm{h},e}}{\partial \boldsymbol{\xi}} = \sum_{i=1}^{8} \mathbf{X}^e_i \otimes \nabla_{\xi} N_i, \qquad (16)$$

respectively. Therein, N_i are the standard *trilinear Lagrangian* shape functions and $\boldsymbol{\xi} \in \hat{\Omega} = [-1, +1]^3$ denotes the *isoparametric coordinates* defined on the reference element $\hat{\Omega}$.

Another set of coordinates, which is extensively used for the ansatz spaces described in Section 3.2, are the *skew coordinates*. They were first proposed by Yuan et al.[67] and Wisniewski and Turska[68] in the context of assumed stress elements and are given by

$$\bar{\boldsymbol{\xi}} = \begin{bmatrix} \bar{\xi} & \bar{\eta} & \bar{\zeta} \end{bmatrix}^{\mathrm{T}} = \mathbf{J}_0^{-1} \left(\mathbf{X}^{\mathrm{h},e} - \mathbf{X}_0 \right), \qquad (17)$$

where

$$\mathbf{J}_0 = \mathbf{J}^{\mathrm{h},e}(\mathbf{0}), \qquad \mathbf{X}_0 = \mathbf{X}^{\mathrm{h},e}(\mathbf{0}) \qquad (18)$$

are the Jacobian and position defined in (16) evaluated at the element center $\boldsymbol{\xi} = \mathbf{0}$. An alternative form of the skew coordinates which directly links them to the isoparametric coordinates is given by Pfefferkorn and Betsch[18]

$$\bar{\boldsymbol{\xi}} = \boldsymbol{\xi} + \sum_{A=1}^{4} \mathbf{c}^A H_A(\boldsymbol{\xi}), \tag{19}$$

and is based on an alternative representation of the shape functions (see e.g., References[16,69,70]). In the equation above we use

$$\mathbf{c}^A = \mathbf{J}_0^{-1} \frac{1}{8} \sum_{i=1}^{8} \mathbf{X}_i^e h_i^A, \tag{20a}$$

$$H_1 = \eta\zeta, \qquad H_2 = \xi\zeta, \qquad H_3 = \xi\eta, \qquad H_4 = \xi\eta\zeta, \tag{20b}$$

$$\begin{aligned} \mathbf{h}^1 &= \begin{bmatrix} +1 & +1 & -1 & -1 & -1 & -1 & +1 & +1 \end{bmatrix}^{\mathrm{T}}, \\ \mathbf{h}^2 &= \begin{bmatrix} +1 & -1 & -1 & +1 & -1 & +1 & +1 & -1 \end{bmatrix}^{\mathrm{T}}, \\ \mathbf{h}^3 &= \begin{bmatrix} +1 & -1 & +1 & -1 & +1 & -1 & +1 & -1 \end{bmatrix}^{\mathrm{T}}, \\ \mathbf{h}^4 &= \begin{bmatrix} -1 & +1 & -1 & +1 & +1 & -1 & +1 & -1 \end{bmatrix}^{\mathrm{T}}. \end{aligned} \tag{20c}$$

The most important properties of the skew coordinate map (17) are its frame-indifference (see Section 4.2) and the fact that (17) is an affine map of the physical coordinates. These features facilitate the construction of proper ansatz spaces. More details on the skew coordinate frame can, for example, be found in the work of Pfefferkorn and Betsch.[18]

3.2 | Ansatz spaces

3.2.1 | Test function for the deformation

For the ansatz of the test function of the deformation $\delta\boldsymbol{\varphi}^{\mathrm{h},e} \in \mathcal{V}^{\mathrm{h}}$ we use the standard isoparametric concept such that

$$\delta\boldsymbol{\varphi}^{\mathrm{h},e} = \sum_{i=1}^{8} N_i \delta\boldsymbol{\varphi}_i^e \tag{21}$$

is defined in the same way as (16) with the same trilinear Lagrangian shape functions N_i and the nodal weights $\delta\boldsymbol{\varphi}_i^e$. For the discrete spatial gradient of $\delta\boldsymbol{\varphi}^{\mathrm{h},e}$ we define

$$\bar{\nabla}_{\mathbf{x}} \delta\boldsymbol{\varphi}^{\mathrm{h},e} = \nabla_{\mathbf{X}} \delta\boldsymbol{\varphi}^{\mathrm{h},e} \mathbf{F}_0^{-1}, \tag{22}$$

$$\mathbf{F}_0 = \mathbf{F}_{\varphi}^{\mathrm{h},e}\big|_{\xi=\mathbf{0}}, \tag{23}$$

in analogy to (13). Therein, $\mathbf{F}_{\varphi}^{\mathrm{h},e}$ denotes the compatible deformation gradient which is subsequently defined in (28) and $\mathbf{F}_0$ is its evaluation at the element center $\boldsymbol{\xi} = \mathbf{0}$. Employing $\mathbf{F}_0$ in (22) ensures consistency with ordinary continuum mechanics as well as objectivity of the finite element (see Sections 4.1 and 4.2).

3.2.2 | Trial function for the deformation

The next field to be discretized is the trial function of the deformation $\boldsymbol{\varphi}^{\mathrm{h},e} \in \mathcal{U}^{\mathrm{h}}$. Similarly to the approximation of the test function (21) we use

$$\boldsymbol{\varphi}^{\mathrm{h},e} = \sum_{i=1}^{8} M_i^e \boldsymbol{\varphi}_i^e, \tag{24}$$

where $\boldsymbol{\varphi}_i^e$ are the nodal weights. The only difference to the discretization of the test function (21) is that (24) uses the *metric shape functions* M_i^e instead of the isoparametric N_i. This alternative set of shape functions is constructed elementwise in the physical space[§] using the skew coordinates (17). For a hexahedral element Ω_0^e the metric shape functions M_i^e are a linear combination of the eight monomials $1, \bar{\xi}, \bar{\eta}, \bar{\zeta}, \bar{\xi}\bar{\eta}, \bar{\eta}\bar{\zeta}, \bar{\zeta}\bar{\xi}, \bar{\xi}\bar{\eta}\bar{\zeta}$ and given by

$$\begin{bmatrix} M_1^e & \cdots & M_8^e \end{bmatrix} = \begin{bmatrix} 1 & \bar{\xi} & \bar{\eta} & \cdots & \bar{\xi}\bar{\eta}\bar{\zeta} \end{bmatrix} \left(\mathbf{A}_{\bar{\xi}} \right)^{-1}, \qquad \mathbf{A}_{\bar{\xi}} = \begin{bmatrix} 1 & \bar{\xi}_1 & \bar{\eta}_1 & \cdots & \bar{\xi}_1\bar{\eta}_1\bar{\zeta}_1 \\ & \vdots & & \ddots & \vdots \\ 1 & \bar{\xi}_8 & \bar{\eta}_8 & \cdots & \bar{\xi}_8\bar{\eta}_8\bar{\zeta}_8 \end{bmatrix}, \tag{25}$$

where $\bar{\boldsymbol{\xi}}_j^e$ are the skew coordinates of the nodes. Relation (25) can be established by enforcing the Kronecker-delta property $M_i^e(\bar{\boldsymbol{\xi}}_j^e) = \delta_{ij}$ at all eight nodes.[18] Vice versa, evaluating (25) at the nodes yields

$$\begin{bmatrix} M_1^e(\bar{\boldsymbol{\xi}}_1) & \cdots & M_8^e(\bar{\boldsymbol{\xi}}_1) \\ \vdots & \ddots & \vdots \\ M_1^e(\bar{\boldsymbol{\xi}}_8) & \cdots & M_8^e(\bar{\boldsymbol{\xi}}_8) \end{bmatrix} = \mathbf{A}_{\bar{\xi}} \left(\mathbf{A}_{\bar{\xi}} \right)^{-1} = \mathbf{I}_{8\times 8}. \tag{26}$$

The derivatives of the metric shape functions (25) with respect to the skew coordinates can be computed in a straightforward way from (25) and are given by

$$\begin{bmatrix} \nabla_{\bar{\xi}} M_1^e & \cdots & \nabla_{\bar{\xi}} M_8^e \end{bmatrix} = \begin{bmatrix} 0 & 1 & 0 & 0 & \bar{\eta} & 0 & \bar{\zeta} & \bar{\eta}\bar{\zeta} \\ 0 & 0 & 1 & 0 & \bar{\xi} & \bar{\zeta} & 0 & \bar{\xi}\bar{\zeta} \\ 0 & 0 & 0 & 1 & 0 & \bar{\eta} & \bar{\xi} & \bar{\xi}\bar{\eta} \end{bmatrix} \left(\mathbf{A}_{\bar{\xi}} \right)^{-1}. \tag{27}$$

The inverse matrix $(\mathbf{A}_{\bar{\xi}})^{-1}$ used in both (25) and (27) exists as long as there are no coincident nodes and the element's volume does not vanish. Fortunately, the computationally expensive task of evaluating (25) and (27) for every element has to be conducted only once at problem initialization and the results can be stored for all further Newton iterations and load steps. This is because the skew coordinates (17) are defined in terms of the constant reference coordinates rather than the current configuration used, for example, by Li et al.[41] Therefore, the increased numerical effort to compute the metric shape functions is hardly relevant in nonlinear simulations.

Further important properties of the metric shape functions are their frame-indifference and isotropy[¶] due to the use of the skew coordinates. On top of that M_i^e are a partition of unity $\sum_{i=1}^8 M_i^e = 1$, have by construction the Kronecker-delta property (26) and, in case of a constant Jacobian $\mathbf{J}^{\mathrm{h},e} = \mathbf{J}_0$, the metric shape functions M_i^e coincide with their isoparametric counter parts N_i. Finally and most importantly, their definition in the skew space enables the construction of complete ansatz functions in the physical space (see Section 3.2.3).

Returning to (24) the metric shape functions (25) define the discrete trial function of the deformation and allow to compute corresponding kinematic fields. First, in view of (2), the discrete displacement-based deformation gradient can now be written as

$$\mathbf{F}_{\varphi}^{\mathrm{h},e} = \sum_{i=1}^{8} \boldsymbol{\varphi}_i^e \otimes \nabla_{\mathbf{X}} M_i^e, \tag{28}$$

where the derivatives of the metric shape functions M_i^e with respect to the reference coordinates $\mathbf{X}$ can easily be determined from (27), (17) and the chain rule such that

$$\nabla_{\mathbf{X}} M_i^e = \mathbf{J}_0^{-\mathrm{T}} \nabla_{\bar{\xi}} M_i^e. \tag{29}$$

Second, with relations (28) and (5) at hand the discrete compatible part $\mathbf{h}_{\varphi}^{\mathrm{h},e}$ of the displacement gradient (10) can be written as

$$\mathbf{h}_{\varphi}^{\mathrm{h},e} = \mathbf{I} - \left(\mathbf{F}_{\varphi}^{\mathrm{h},e} \right)^{-1}. \tag{30}$$

3.2.3 | Trial function for the enhanced strain

The enhanced part $\tilde{\mathbf{h}}^{\mathrm{h},e} \in \mathcal{E}^{\mathrm{h}}$ of the total displacement gradient (10) and the corresponding test function (see Section 3.2.4) are approximated elementwise which facilitates static condensation of the additional degrees of freedom on element level. To ensure objectivity and to pass the patch test (see Sections 4.2 and 4.6) we propose the form

$$\tilde{\mathbf{h}}^{\mathrm{h},e} = \overline{\mathbf{h}}^{\mathrm{h},e}(\boldsymbol{\alpha}^e)\mathbf{F}_0^{-1}, \tag{31}$$

where $\mathbf{F}_0$ denotes the compatible deformation gradient $\mathbf{F}_{\varphi}^{\mathrm{h},e}$ at the element center $\boldsymbol{\xi} = \mathbf{0}$ (see (23)) and $\overline{\mathbf{h}}^{\mathrm{h},e} = \overline{\mathbf{h}}_1^{\mathrm{h},e} + \overline{\mathbf{h}}_2^{\mathrm{h},e}$ includes the incompatible degrees of freedom $\boldsymbol{\alpha}^e$ and consists of two parts.

The first set of enhanced ansatz functions is motivated by examining (25) which reveals that the three monomials $\tilde{m}_1^e = \overline{\xi}^2$, $\tilde{m}_2^e = \overline{\eta}^2$, and $\tilde{m}_3^e = \overline{\zeta}^2$ are missing for a fully quadratic deformation field. However, as shown by Pfefferkorn and Betsch,[18] the functions $\tilde{m}_j^e, j = 1, 2, 3$ cannot be used directly in the form of incompatible modes. The modification

$$\tilde{M}_j^e = \tilde{m}_j^e(\overline{\boldsymbol{\xi}}) - \sum_{i=1}^{8} M_i^e(\overline{\boldsymbol{\xi}})\tilde{m}_j^e(\overline{\boldsymbol{\xi}}_i), \qquad j = 1, 2, 3 \tag{32}$$

is necessary to ensure that the incompatible displacements do not contribute to the nodal deformations, that is, $\tilde{M}_j^e(\overline{\boldsymbol{\xi}}_i) = 0$ holds. Thus, (32) ensures that $\boldsymbol{\varphi}_i^e$ introduced in (24) are actual nodal deformations. Moreover, the modified functions $\tilde{M}_j^e$ coincide with the bubble functions by Wilson et al.[3] in case of undistorted meshes.[18] Ultimately, (32) can be used in the sense of incompatible modes for $\overline{\mathbf{h}}^{\mathrm{h},e}$ which yields

$$\overline{\mathbf{h}}_1^{\mathrm{h},e} = \sum_{j=1}^{3} \boldsymbol{\alpha}_j^e \otimes \nabla_{\mathbf{X}} \tilde{M}_j^e \tag{33}$$

and has the same structure as the approximation of the deformation gradient in (28). The last equation implies that $\overline{\mathbf{h}}_1^{\mathrm{h},e}$ includes three incompatible displacement modes with a total of nine additional degrees of freedom arranged in the vectors $\boldsymbol{\alpha}_j^e$, $j = 1, 2, 3$.

The second set of enhanced modes contains three modes and is necessary to avoid a mild form of volumetric locking.[5,18] For the present finite element we use the modes

$$\overline{\mathbf{h}}_2^{\mathrm{h},e} = \mathbf{J}_0^{-\mathrm{T}} \begin{bmatrix} \alpha_{11}^e \overline{\xi\zeta} + \alpha_{12}^e \overline{\xi}\overline{\eta} & 0 & 0 \\ 0 & \alpha_{10}^e \overline{\eta\zeta} + \alpha_{12}^e \overline{\xi}\overline{\eta} & 0 \\ 0 & 0 & \alpha_{10}^e \overline{\eta\zeta} + \alpha_{11}^e \overline{\xi\zeta} \end{bmatrix} \mathbf{J}_0^{-1}, \tag{34}$$

which are defined in terms of skew coordinates and represent a slight modification of the modes used by Pfefferkorn and Betsch.[18] This modification is inspired by the analytic solutions for linear elastic higher order displacement modes presented in Appendix A and its major advantage is that it allows to circumvent the need for an orthogonalization procedure as is further outlined in Section 3.2.4.

3.2.4 | Test function for the enhanced strain

The last field which has to be discretized is the test function for the enhanced strain $\delta\tilde{\mathbf{h}}^{\mathrm{h},e} \in \mathcal{F}^{\mathrm{h}}$. Here we assume the form

$$\delta\tilde{\mathbf{h}}^{\mathrm{h},e} = \mathbf{F}_0 \delta\overline{\mathbf{h}}^{\mathrm{h},e} \mathbf{F}_0^{\mathrm{T}}, \tag{35}$$

where again the deformation gradient at the element center (23) is employed for objectivity (see Section 4.2). Moreover, $\delta\overline{\mathbf{h}}^{\mathrm{h},e}$ is given by

$$\delta\overline{\mathbf{h}}^{\mathrm{h},e} = \frac{1}{j^{\mathrm{h},e}} \mathbf{J}_0^{-\mathrm{T}} \delta\hat{\mathbf{h}}^{\mathrm{h},e} \mathbf{J}_0^{-1}, \tag{36}$$

where $j^{\mathrm{h},e} = \det(\mathbf{J}^{\mathrm{h},e})$ and $\mathbf{J}_0$ is defined in (18). The last equation includes the transformation from the reference element $\hat{\Omega}$ to the physical configuration Ω_0^e and has the same structure as the test function for the incompatible strain introduced by Pfefferkorn and Betsch[18] (see also Simo and Rifai[1]). In view of the symmetry of $\hat{\boldsymbol{\tau}}^{\mathrm{h},e}$ and the transformations given in (35) and (36) the skew-symmetric contribution of $\delta\hat{\mathbf{h}}^{\mathrm{h},e}$ is immaterial in (15b). For the symmetric part we assume the form

$$\delta\hat{\mathbf{h}}_v^{\mathrm{h},e} = \left[\begin{array}{ccc|ccccccc} \xi & 0 & 0 & 0 & 0 & 0 & 0 & 0 & 0 \\ 0 & \eta & 0 & 0 & 0 & 0 & 0 & 0 & 0 \\ 0 & 0 & \zeta & 0 & 0 & 0 & 0 & 0 & 0 \\ 0 & 0 & 0 & \xi & \eta & 0 & 0 & 0 & 0 \\ 0 & 0 & 0 & 0 & 0 & \eta & \zeta & 0 & 0 \\ 0 & 0 & 0 & 0 & 0 & 0 & 0 & \xi & \zeta \end{array}\right| \left[\begin{array}{ccc} 0 & \xi\zeta - \hat{h}_{11}^1 & \xi\eta - \hat{h}_{12}^1 \\ \eta\zeta - \hat{h}_{10}^2 & 0 & \xi\eta - \hat{h}_{12}^2 \\ \eta\zeta - \hat{h}_{10}^3 & \xi\zeta - \hat{h}_{11}^3 & 0 \\ 0 & 0 & 0 \\ 0 & 0 & 0 \\ 0 & 0 & 0 \end{array}\right] \left[\begin{array}{c} \alpha_1 \\ \alpha_2 \\ \vdots \\ \alpha_{12} \end{array}\right], \tag{37a}$$

$$\begin{aligned} \hat{h}_{10}^2 &= \tfrac{1}{3}(\xi c_1^1 - \zeta c_3^1), \qquad \hat{h}_{11}^1 = \tfrac{1}{3}(\eta c_2^2 - \zeta c_3^2), \qquad \hat{h}_{12}^1 = \tfrac{1}{3}(\zeta c_3^3 - \eta c_2^3), \\ \hat{h}_{10}^3 &= \tfrac{1}{3}(\xi c_1^1 - \eta c_2^1), \qquad \hat{h}_{11}^3 = \tfrac{1}{3}(\eta c_2^2 - \xi c_1^2), \qquad \hat{h}_{12}^2 = \tfrac{1}{3}(\zeta c_3^3 - \xi c_1^3), \end{aligned} \tag{37b}$$

where $(\bullet)_v$ denotes vector-matrix notation and $\hat{h}_j^i$ are correction terms which ensure orthogonality with the analytic stress modes given subsequently in (58). The corrections are computed using components of the vectors $\mathbf{c}^A$ defined in (20a) which vanish in case of regular meshes. The modes in the equation above are a modification of the ones proposed by Pfefferkorn and Betsch[18] and motivated by the analytic solutions for linear elasticity presented in Appendix A. Ultimately, the modification allows to skip the time consuming and intricate *orthogonalization procedure* employed in the work[18] while maintaining the high performance of the element. Thus, using the modified (37) is a valuable improvement of the element proposed by Pfefferkorn and Betsch.[18]

3.2.5 | Total displacement and deformation gradient

In view of the approximations (30), (31) and the kinematic relations (10), (11) the discrete total deformation and displacement gradient required to compute the constitutive stress can be written as

$$\mathbf{h}^{\mathrm{h},e} = \mathbf{h}_\varphi^{\mathrm{h},e} + \tilde{\mathbf{h}}^{\mathrm{h},e}, \tag{38}$$

$$\mathbf{F}^{\mathrm{h},e} = \left(\mathbf{I} - \mathbf{h}^{\mathrm{h},e}\right)^{-1}. \tag{39}$$

3.3 | Alternative ansatz spaces

In this section, we present a short outline of alternative approaches for the extension of our previous work[18] to the large deformation regime.

3.3.1 | Enhancement of $\mathbf{h}$

The ansatz spaces presented for the element in Section 3.2 are not the only possible choices. For instance, many other transformations to ensure objectivity in (22), (31), and (35) would be possible. Furthermore, there exist a plethora of other ansatz functions for enhanced fields such as, for example, the transposed Wilson-modes first proposed by Korelc and Wriggers.[7]

However, our numerical experiments suggest that the element described in Section 3.2 has the most favorable behavior. All other tested elements exhibit spurious instabilities, perform worse with mesh distortion or have other serious drawbacks. In particular, elements which use either $\mathbf{F}^{\mathrm{h},e}$ or $(\mathbf{F}^{\mathrm{h},e})^{-\mathrm{T}}$ instead of $\mathbf{F}_0$ in (35) exhibit hourglassing modes similar to the standard EAS element.[2] Replacing $\mathbf{F}_0$ with $\mathbf{F}_0^{-\mathrm{T}}$ in (35) leads to a form of hourglassing under tension for distorted

meshes similar to the one observed in the work[17] for a special transformation for standard EAS elements. Employing $\mathbf{F}^{\mathrm{h},e}$ instead of $\mathbf{F}_0$ in (22) leads to hourglassing under compression for slender elements. Proceeding similarly by replacing $\mathbf{F}_0$ in (22) with $\mathbf{F}_\varphi^{\mathrm{h},e}$ induces spurious modes under tension in case of instable materials. Finally, using the transposed Wilson-modes leads to worse performance with mesh distortion and also induces hourglassing under tension if there are material instabilities.

3.3.2 | Enhancement of $\mathbf{F}$

As pointed out in the introduction and Remark 3 other fields than $\mathbf{h}$ can be enhanced even though this seems to lead to less well performing elements and in particular hourglassing instabilities. This section briefly summarizes a possible PG-EAS discretization for elements based on enhancement of the deformation gradient $\mathbf{F}$ (9) and the corresponding weak form (14).

To that end we first chose a stress field $\mathbf{P}^{\mathrm{h}}$ which is L_2-orthogonal to the incompatible strain $\tilde{\mathbf{F}}^{\mathrm{h}}$ in order to get a discrete weak form similar to (15). Second, the approximations for the test and trial functions of the deformation are chosen exactly the same as presented in Section 3.2. Thus, $\delta\boldsymbol{\varphi}^{\mathrm{h},e}$ and $\boldsymbol{\varphi}^{\mathrm{h},e}$ are approximated according to (21) and (24), respectively. Finally, for the test and trial function of the enhanced deformation gradient suitable choices are

$$\tilde{\mathbf{F}}^{\mathrm{h},e} = \mathbf{F}_\varphi^{\mathrm{h},e}\overline{\mathbf{F}}^{\mathrm{h},e}, \tag{40a}$$

$$\delta\tilde{\mathbf{F}}^{\mathrm{h},e} = (\mathbf{F}^{\mathrm{h},e})^{-\mathrm{T}}\delta\overline{\mathbf{F}}^{\mathrm{h},e}, \tag{40b}$$

where in both equations the first factor ensures objectivity and the second contains the actual ansatz functions for the respective field. In particular, we consider an element that uses the Wilson-modes, that is, (33) and (36), for $\overline{\mathbf{F}}^{\mathrm{h},e}$ and $\delta\overline{\mathbf{F}}^{\mathrm{h},e}$, respectively. Furthermore, we also test an element that uses the transposed Wilson-modes only for $\overline{\mathbf{F}}^{\mathrm{h},e}$ in the numerical studies in Section 5.

3.3.3 | Enhancement of $\mathbf{E}$

The simplest nonlinear EAS element in terms of finding a suitable discretization is the one based on enhancement of the Green–Lagrange strain $\mathbf{E}$ and its work-conjugate second Piola-Kirchhoff stress $\mathbf{S}$. Since both these fields are defined in the reference configuration no modifications are necessary for objectivity and it is possible to take the ansatz spaces from the work[18] without adaptions. Unfortunately, these elements suffer from spurious instabilities (see Section 5.6).

3.4 | MIP method for increased robustness

One deficiency of EAS elements is their lack of *robustness*,[19] by which we mean the high number of load steps and Newton iterations required for convergence in comparison to assumed stress elements. Pfefferkorn et al.[19] extend the *mixed integration point* (MIP) method proposed by Magisano et al.[30] to EAS elements which considerably increases their robustness in many examples. The key idea of that method is to introduce an independent stress tensor $\mathbf{S}_g$ at every Gauss point $g = 1, \ldots, n_{\mathrm{gp}}$. Static condensation of $\mathbf{S}_g$ leads then to a modified element stiffness matrix where the constitutive stress in the geometric parts of the tangent is replaced with the independent stress at the Gauss points.

In the present work we employ the MIP method as presented by Pfefferkorn et al.[19] We refer to aforementioned reference for details on the implementation (see especially Section 5 in Reference 19) and our numerical simulation in Section 5.5 for the effect of the MIP approach.

4 | FEATURES AND PROPERTIES OF H1U/H12

The element proposed in Sections 2 and 3 is named **H1U/h12** which stands for a (tri-)linear hexahedral unsymmetric element ("H1U"), with twelve h-enhanced modes ("h12"). In this section, we prove that H1U/h12 has many interesting

features which lead to the high performance in numerical simulations covered in Section 5. The most important features are the improved accuracy in case of distorted meshes discussed in Section 4.5 and the increased stability covered in Sections 4.8 and 4.9. All properties presented in this section are also verified numerically in Section 5.

4.1 | Consistency with ordinary continuum mechanics

In a first step we analyze the mixed weak form (12). To ensure that the proposed weak form is a suitable basis for the construction of a finite element we have to show that it is *consistent* with ordinary continuum mechanics. This ensures that a mixed finite element formulation based on (12) converges to the analytic results with mesh refinement provided that there are no instabilities, the solution is sufficiently regular and the patch test (see Section 4.6) is fulfilled.

To prove consistency of the weak form (12) it is sufficient to show that it can be reduced to a purely displacement-based formulation in a continuous (non-discrete) setting. To that end we first obtain from (12c) and the standard localization argument $\tilde{\mathbf{h}} = \mathbf{0}$. In view of (10), (5), and (6) we then immediately get $\hat{\boldsymbol{\tau}} = \hat{\boldsymbol{\tau}}_\varphi$ meaning that the constitutive stress does not depend on the additional field $\tilde{\mathbf{h}}$. Inserting this result into (12b) reveals $\boldsymbol{\tau} = \hat{\boldsymbol{\tau}}_\varphi$. Finally using $\tilde{\mathbf{h}} = \mathbf{0}$ together with (13) and (7) in (12a) yields

$$\int_{\mathcal{B}_0} \tilde{\nabla}^{\mathrm{s}}_{\mathbf{x}} \delta\boldsymbol{\varphi} \,:\, \hat{\boldsymbol{\tau}} \mathrm{d}V = \int_{\mathcal{B}_0} \nabla_{\mathbf{X}} \delta\boldsymbol{\varphi} \,:\, \hat{\mathbf{P}}_\varphi \mathrm{d}V = -G_{\mathrm{ext}}(\delta\boldsymbol{\varphi}), \tag{41}$$

which is exactly the same as the standard displacement-based weak form. Thus, the weak form postulated in (12) is consistent with ordinary continuum mechanics and a suitable basis for the novel finite element framework.

4.2 | Frame invariance and objectivity

Next we thoroughly show that the discrete weak form (15) and consequently the novel element H1U/h12 is invariant to a global change of reference coordinates $(\bullet)^\flat$ (*frame-invariance*) and a superimposed rigid body motion $(\bullet)^\sharp$ (*objectivity*). The corresponding transformations are

$$\mathbf{X}^\flat = \mathbf{R}\mathbf{X} + \mathbf{c}, \tag{42a}$$

$$\boldsymbol{\varphi}^\sharp = \mathbf{Q}\boldsymbol{\varphi} + \mathbf{d}, \tag{42b}$$

where $\mathbf{R}, \mathbf{Q} \in \mathcal{SO}(3)$ are proper orthogonal tensors and $\mathbf{c}, \mathbf{d} \in \mathbb{R}^3$. First, we consider changes of element geometry described in Section 3.1 due to (42a) and note that transformation (42a) implies nodal coordinate changes according to $\mathbf{X}_i^{e,\flat} = \mathbf{R}\mathbf{X}_i^e + \mathbf{c}$. In view of (16) this means $\mathbf{X}^{\mathrm{h},e,\flat} = \mathbf{R}\mathbf{X}^{\mathrm{h},e} + \mathbf{c}$ and $\mathbf{J}^{\mathrm{h},e,\flat} = \mathbf{R}\mathbf{J}^{\mathrm{h},e}$ which yields

$$\bar{\boldsymbol{\xi}}^\flat = (\mathbf{J}_0^\flat)^{-1} \left(\mathbf{X}^{\mathrm{h},e,\flat} - \mathbf{X}_0^\flat \right) = \mathbf{J}_0^{-1}\mathbf{R}^{-1}\mathbf{R} \left(\mathbf{X}^{\mathrm{h},e} - \mathbf{X}_0 \right) = \bar{\boldsymbol{\xi}} \tag{43}$$

for the skew coordinates (17). Thus, the skew coordinates are frame-invariant analogous to the isoparametric frame $\boldsymbol{\xi}^\flat = \boldsymbol{\xi}$ and therefore a suitable basis for the construction of ansatz spaces. Moreover, according to (29),

$$(\nabla_{\mathbf{X}}(\bullet))^\flat = \left(\mathbf{J}_0^\flat \right)^{-\mathrm{T}} \nabla_{\bar{\boldsymbol{\xi}}}(\bullet) = \mathbf{R}\nabla_{\mathbf{X}}(\bullet), \qquad (\nabla_{\mathbf{X}}(\bullet))^\flat = \left(\mathbf{J}^\flat \right)^{-\mathrm{T}} \nabla_{\boldsymbol{\xi}}(\bullet) = \mathbf{R}\nabla_{\mathbf{X}}(\bullet), \tag{44}$$

holds similarly for fields based on skew and isoparametric coordinates. Second, we consider changes of kinematic fields due to (42). By aid of (5), (42), (44) and $\boldsymbol{\varphi}^{\mathrm{h},e,\sharp} = \mathbf{Q}\boldsymbol{\varphi}^{\mathrm{h},e} + \mathbf{d}$ the discrete displacement-based deformation gradient (28) and the corresponding displacement gradient (30) transform according to

$$\mathbf{F}_\varphi^{\mathrm{h},e,\sharp} = \frac{\partial \boldsymbol{\varphi}^{\mathrm{h},e,\sharp}}{\partial \mathbf{X}^{\mathrm{h},e,\flat}} = \mathbf{Q}\mathbf{F}_\varphi^{\mathrm{h},e}\mathbf{R}^{\mathrm{T}}, \tag{45}$$

$$\mathbf{h}_\varphi^{\mathrm{h},e,\sharp} = \mathbf{I} - \left(\mathbf{F}_\varphi^{\mathrm{h},e,\sharp} \right)^{-1} = \mathbf{I} - \mathbf{R} \left(\mathbf{I} - \mathbf{h}_\varphi^{\mathrm{h},e} \right) \mathbf{Q}^{\mathrm{T}}. \tag{46}$$

Furthermore, under the assumption that the incompatible degrees of freedom in (33) and (34) transform via $\boldsymbol{\alpha}_j^{e,\sharp} = \mathbf{R}\boldsymbol{\alpha}_j^e$, $j = 1, 2, 3$ and $\alpha_k^{e,\sharp} = \alpha_k^e$, $k = 10, 11, 12$, respectively, the transformation of the enhanced part of the displacement gradient (31) is given by

$$\tilde{\mathbf{h}}^{\mathrm{h},e,\sharp} = \overline{\mathbf{h}}^{\mathrm{h},e,\sharp}\left(\mathbf{F}_0^{\sharp}\right)^{-1} = \mathbf{R}\overline{\mathbf{h}}^{\mathrm{h},e}\mathbf{R}^{\mathrm{T}}\mathbf{R}\mathbf{F}_0^{-1}\mathbf{Q}^{\mathrm{T}} = \mathbf{R}\tilde{\mathbf{h}}^{\mathrm{h},e}\mathbf{Q}^{\mathrm{T}}. \tag{47}$$

Combining transformations (46) and (47) with (38) and (39) yields the transformation for the total deformation gradient

$$\mathbf{F}^{\mathrm{h},e,\sharp} = \left(\mathbf{I} - \mathbf{h}_{\varphi}^{\mathrm{h},e,\sharp} - \tilde{\mathbf{h}}^{\mathrm{h},e,\sharp}\right)^{-1} = \left(\mathbf{R}\left(\mathbf{I} - \mathbf{h}_{\varphi}^{\mathrm{h},e} - \tilde{\mathbf{h}}^{\mathrm{h},e}\right)\mathbf{Q}^{\mathrm{T}}\right)^{-1} = \mathbf{Q}\mathbf{F}^{\mathrm{h},e}\mathbf{R}^{\mathrm{T}}, \tag{48}$$

which is the same as (45) and in particular the correct transformation for a deformation gradient (see e.g., Ogden[71]). This is only possible because of $\mathbf{F}_0$ included in (31) which ensures proper transformation of the enhanced displacement gradient. Third, for a proper isotropic elastic material (48) implies that the constitutive Kirchhoff stress tensor transforms according to

$$\hat{\boldsymbol{\tau}}(\mathbf{F}^{\mathrm{h},e,\sharp}) = \hat{\boldsymbol{\tau}}(\mathbf{Q}\mathbf{F}^{\mathrm{h},e}\mathbf{R}^{\mathrm{T}}) = \hat{\boldsymbol{\tau}}(\mathbf{Q}\mathbf{F}^{\mathrm{h},e}) = \mathbf{Q}\hat{\boldsymbol{\tau}}(\mathbf{F}^{\mathrm{h},e})\mathbf{Q}^{\mathrm{T}}, \tag{49}$$

where the second equality holds because of *isotropy* and the third is due to *material objectivity* (see e.g., Haupt[72] Chapter 7.2 and 7.3). Now, the only expressions in (15) whose transformations have not been established are the test functions. According to (21), (22), (35), and (36) we obtain

$$\left(\tilde{\nabla}\delta\boldsymbol{\varphi}^{\mathrm{h},e}\right)^{\sharp} = \nabla_{\mathbf{X}}\delta\boldsymbol{\varphi}^{\mathrm{h},e,\sharp}\left(\mathbf{F}_0^{\sharp}\right)^{-1} = \mathbf{Q}\nabla_{\mathbf{X}}\delta\boldsymbol{\varphi}^{\mathrm{h},e}\mathbf{R}^{\mathrm{T}}\mathbf{R}(\mathbf{F}_0)^{-1}\mathbf{Q}^{\mathrm{T}} = \mathbf{Q}\tilde{\nabla}\delta\boldsymbol{\varphi}^{\mathrm{h},e}\mathbf{Q}^{\mathrm{T}}, \tag{50}$$

$$\delta\tilde{\mathbf{h}}^{\mathrm{h},e,\sharp} = \mathbf{F}_0^{\sharp}\frac{1}{j^{\mathrm{h},e,\sharp}}\left(\mathbf{J}_0^{\sharp}\right)^{-\mathrm{T}}\delta\hat{\mathbf{h}}^{\mathrm{h},e,\sharp}\left(\mathbf{J}_0^{\sharp}\right)^{-1}\left(\mathbf{F}_0^{\sharp}\right)^{\mathrm{T}} = \mathbf{Q}\delta\tilde{\mathbf{h}}^{\mathrm{h},e}\mathbf{Q}^{\mathrm{T}} \tag{51}$$

by considering the transformations $\delta\boldsymbol{\varphi}^{\mathrm{h},e,\sharp} = \mathbf{Q}\delta\boldsymbol{\varphi}^{\mathrm{h},e} + \mathbf{d}$ and $\delta\overline{\mathbf{h}}^{\mathrm{h},e,\sharp} = \delta\overline{\mathbf{h}}^{\mathrm{h},e}$. In the last two equations the correct transformation is possible due to the proper use of $\mathbf{F}_0$ and $\mathbf{J}_0$ in (22), (35), and (36), respectively.

Finally, substituting (49), (50), and (51) into the internal parts of (15) yields

$$G_{\mathrm{int},\varphi}^{\mathrm{h},e,\sharp} = \int_{\Omega_0^{e,\sharp}} \left(\tilde{\nabla}_{\mathbf{x}}^{\mathrm{s}}\delta\boldsymbol{\varphi}^{\mathrm{h},e}\right)^{\sharp} : \hat{\boldsymbol{\tau}}^{\mathrm{h},e,\sharp}\mathrm{d}V^{\sharp} = \int_{\Omega_0^e} \left(\tilde{\nabla}_{\mathbf{x}}^{\mathrm{s}}\delta\boldsymbol{\varphi}^{\mathrm{h},e}\right) : \hat{\boldsymbol{\tau}}^{\mathrm{h},e}\mathrm{d}V = G_{\mathrm{int},\varphi}^{\mathrm{h},e}, \tag{52a}$$

$$G_{\alpha}^{\mathrm{h},e,\sharp} = \int_{\Omega_0^{e,\sharp}} \delta\tilde{\mathbf{h}}^{\mathrm{h},e,\sharp} : \hat{\boldsymbol{\tau}}^{\mathrm{h},e,\sharp}\mathrm{d}V^{\sharp} = \int_{\Omega_0^e} \delta\tilde{\mathbf{h}}^{\mathrm{h},e} : \hat{\boldsymbol{\tau}}^{\mathrm{h},e}\mathrm{d}V = G_{\alpha}^{\mathrm{h},e}, \tag{52b}$$

which establishes the frame-invariance and objectivity of the novel element H1U/h12 provided that the external loads transform appropriately. Numerical verifications of this proof can be found in Sections 5.1.2 and 5.1.3.

4.3 | Isotropy and path independence

Two further crucial properties for any finite element are *isotropy*, implying invariance to node numbering, and *path-independence* in the case of elastic materials.

Isotropy of H1U/h12 can easily be verified by observing that there are no preferred directions in the ansatz spaces chosen in Section 3.2. Thus, H1U/h12 is invariant to node numbering which is shown numerically in Section 5.1.2. Examples for anisotropic finite elements are the unsymmetric displacement-based element by Ooi et al.[35,36] and the EAS element proposed by Korelc et al.[14] The former is anisotropic because the rotation of the local element coordinates relies only on a subset of nodes and the second is anisotropic because the volumetric enhanced modes have preferred directions.

Another crucial property is *path independence*, that is, that the element does not depend on the deformation history in case of a path-independent material model. As most elements, the current H1U/h12 is path-independent since all ansatz

functions are defined with respect to the reference configuration. If they depend on the current configuration the element is likely to be path-dependent (e.g., the elements by Li et al.[41,42]).

4.4 | Linearized element

In this section, the novel element H1U/h12 is *linearized* and it is shown that its linearization coincides with the highly accurate element proposed by Pfefferkorn and Betsch.[18] The only difference concerns the improved volumetric enhanced modes (34) and (37). Thus, all features of that element such as the much increased coarse mesh accuracy, equivalence to standard EAS elements in case of regular meshes, exact numerical integration of the stiffness matrix by standard Gauss quadrature and, most importantly, the exact solution of many bending problems (see also Section 4.5) carry over to H1U/h12 in case of small deformations.

The weak form (15) is a functional $f : (\boldsymbol{\varphi}, \boldsymbol{\alpha}) \mapsto f(\boldsymbol{\varphi}, \boldsymbol{\alpha})$ of the deformations $\boldsymbol{\varphi}$ and enhanced degrees of freedom $\boldsymbol{\alpha}$. Its linearization in the reference configuration $(\boldsymbol{\varphi}, \boldsymbol{\alpha}) = (\mathbf{X}, \mathbf{0})$ is given by

$$\mathrm{Lin}_{\mathbf{0}} f = f(\mathbf{X}, \mathbf{0}) + \Delta_{\mathbf{0}} f, \qquad \Delta_{\mathbf{0}} f = \frac{\mathrm{d}}{\mathrm{d}\varepsilon} f(\mathbf{X} + \varepsilon \Delta\boldsymbol{\varphi}, \varepsilon \Delta\boldsymbol{\alpha})\Big|_{\varepsilon=0}, \tag{53}$$

where $\Delta\boldsymbol{\varphi}$, $\Delta\boldsymbol{\alpha}$ are increments of the deformation $\boldsymbol{\varphi}$ and enhanced degrees of freedom $\boldsymbol{\alpha}$, respectively. These increments are discretized in the same way as $\boldsymbol{\varphi}$ and $\boldsymbol{\alpha}$ in (21), (33), and (34). Moreover, operator $\Delta_{\mathbf{0}}(\bullet)$ in (53) denotes the Gateaux-derivative of $(\bullet)$ with respect to the increments $\Delta\boldsymbol{\varphi}$, $\Delta\boldsymbol{\alpha}$ evaluated in the reference configuration.

With (30), (28), (31), (33) and relation $\Delta\mathbf{A}^{-1} = -\mathbf{A}^{-1}\Delta\mathbf{A}\mathbf{A}^{-1}$, which holds for the linearization of a arbitrary tensors $\mathbf{A}$,[73] it is then straightforward to obtain

$$\Delta_{\mathbf{0}} \mathbf{h}_{\varphi}^{\mathrm{h},e} = \mathbf{I}^{-1} \Delta_{\mathbf{0}} \mathbf{F}_{\varphi}^{\mathrm{h},e} \mathbf{I}^{-1} = \nabla_{\mathbf{X}} \Delta\boldsymbol{\varphi}^{\mathrm{h},e}, \tag{54a}$$

$$\Delta_{\mathbf{0}} \tilde{\mathbf{h}}^{\mathrm{h},e} = \Delta_{\mathbf{0}} \overline{\mathbf{h}}^{\mathrm{h},e} \mathbf{I} + \mathbf{0} \Delta_{\mathbf{0}} \mathbf{F}_0^{-1} = \overline{\mathbf{h}}^{\mathrm{h},e}(\Delta\boldsymbol{\alpha}^{\mathrm{h},e}) = \overline{\mathbf{h}}_{\Delta\boldsymbol{\alpha}}^{\mathrm{h},e}, \tag{54b}$$

for the compatible and incompatible part of the discrete displacement gradient $\mathbf{h}^{\mathrm{h},e}$, respectively. With this information at hand, linearization of the total deformation gradient (39) yields

$$\Delta_{\mathbf{0}} \mathbf{F}^{\mathrm{h},e} = \nabla_{\mathbf{X}} \Delta\boldsymbol{\varphi}^{\mathrm{h},e} + \overline{\mathbf{h}}_{\Delta\boldsymbol{\alpha}}^{\mathrm{h},e}. \tag{55}$$

Furthermore, linearizing the constitutive stresses (6) under the assumption of an elastic material and by aid of (55) determines

$$\Delta_{\mathbf{0}} \hat{\boldsymbol{\tau}}^{\mathrm{h},e} = \hat{\mathbb{c}}^{\mathrm{h},e}(\mathbf{I}) : \Delta_{\mathbf{0}} \left(\mathbf{F}^{\mathrm{h},e} \left(\mathbf{F}^{\mathrm{h},e} \right)^{\mathrm{T}} \right) = \hat{\mathbb{C}}_{\mathrm{lin}} : \left(\nabla_{\mathbf{X}}^{\mathrm{s}} \Delta\boldsymbol{\varphi}^{\mathrm{h},e} + sym(\overline{\mathbf{h}}_{\Delta\boldsymbol{\alpha}}^{\mathrm{h},e}) \right), \tag{56}$$

where $sym(\overline{\mathbf{h}}_{\Delta\boldsymbol{\alpha}}^{\mathrm{h},e})$ denotes the symmetric part of $\overline{\mathbf{h}}_{\Delta\boldsymbol{\alpha}}^{\mathrm{h},e}$ and $\hat{\mathbb{c}}^{\mathrm{h},e}(\mathbf{F}^{\mathrm{h},e})$ is the constitutive spatial elasticity tensor with the corresponding linear elasticity tensor $\hat{\mathbb{C}}_{\mathrm{lin}} = \hat{\mathbb{c}}^{\mathrm{h},e}(\mathbf{I})$. Finally, with the auxiliary results above, the linearization (53) of the weak form (15) is given by

$$Lin_{\mathbf{0}} G_{\varphi}^{\mathrm{h}} = \int_{\mathcal{B}_0^h} \nabla_{\mathbf{X}}^{\mathrm{s}} \delta\boldsymbol{\varphi}^{\mathrm{h}} : \hat{\mathbb{C}}_{\mathrm{lin}} : \left(\nabla_{\mathbf{X}}^{\mathrm{s}} \Delta\boldsymbol{\varphi}^{\mathrm{h}} + sym(\overline{\mathbf{h}}_{\Delta\boldsymbol{\alpha}}^{\mathrm{h},e}) \right) \mathrm{d}V - G_{\mathrm{ext}}^{\mathrm{h}}(\delta\boldsymbol{\varphi}^{\mathrm{h}}) = 0, \tag{57a}$$

$$Lin_{\mathbf{0}} G_{\alpha}^{\mathrm{h}} = \int_{\mathcal{B}_0^h} \delta\overline{\mathbf{h}}^{\mathrm{h}} : \hat{\mathbb{C}}_{\mathrm{lin}} : \left(\nabla_{\mathbf{X}}^{\mathrm{s}} \Delta\boldsymbol{\varphi}^{\mathrm{h}} + sym(\overline{\mathbf{h}}_{\Delta\boldsymbol{\alpha}}^{\mathrm{h},e}) \right) \mathrm{d}V = 0, \tag{57b}$$

which is the same as the weak form of the standard linear elastic EAS element. Furthermore, the approximation of the fields in Section 3.2 is, apart from the two minor modifications (34) and (37), taken directly from the work of Pfefferkorn and Betsch.[18] Thus, the only differences of the linearized H1U/h12 in comparison to the linear elastic element in aforementioned reference are (34) and (37). The linearization of the corresponding 2D element is even exactly the same as the element proposed in the work.[18]

4.5 | Insensitivity to mesh distortion

This section covers the *design conditions* established by Pfefferkorn and Betsch[18] which allow to construct elements with optimal or close to optimal performance *regardless of mesh distortion*. To that end we first briefly repeat the linear elastic case from Reference 18 and then generalize the concept to nonlinear problems.

4.5.1 | Linear elasticity

For linear elasticity the investigations by MacNeal[18,31] show that an element with N degrees of freedom can at best be exact for N displacement modes provided that its stiffness matrix is unsymmetric. In case of a PG-EAS framework Pfefferkorn and Betsch[18] examined the weak form (57) and obtained *three design conditions* required to get an exact finite element solution for a specific displacement mode regardless of mesh distortion. The design conditions are:[18]

- C1 The test functions for the displacement $\delta\mathbf{u}^{\mathrm{h}}$ have to fulfill the inter-element continuity. This ensures that nodal equilibrium is fulfilled and that the correct solutions for a single element can be generalized to larger patches of elements.
- C2 The ansatz spaces for the displacement $\mathbf{u}^{\mathrm{h},e}$ and incompatible strain $\tilde{\boldsymbol{\varepsilon}}^{\mathrm{h},e}$ must be chosen such that resulting $\hat{\boldsymbol{\sigma}}^{\mathrm{h},e}$ includes the analytic stress $\boldsymbol{\sigma}^*$ under the premise of nodally exact displacements.
- C3 The test function of the incompatible strain $\delta\tilde{\boldsymbol{\varepsilon}}^{\mathrm{h},e}$ must be L_2-orthogonal to the analytic stress $\boldsymbol{\sigma}^*$. This condition is an extension of the patch test condition for EAS elements originally proposed by Simo and Rifai.[1]

These conditions can be used to construct an optimal or close to optimal finite element by choosing a proper set of N analytic modes for which the element is then designed to be exact.[18]

Similar to the work of Pfefferkorn and Betsch[18] we use the stress modes usually employed for assumed stress elements[68,74,75] as analytic modes. They are defined in terms of skew coordinates (17) and given by

$$\boldsymbol{\sigma}^* = \mathbf{J}_0 \bar{\boldsymbol{\sigma}}^* \mathbf{J}_0^{\mathrm{T}}, \tag{58a}$$

$$\bar{\boldsymbol{\sigma}}_v^*(\bar{\boldsymbol{\xi}}) := \left[\begin{array}{cccccc|cccccc|ccc} 1&0&0&0&0&0&\bar{\eta}&\bar{\zeta}&0&0&0&0&0&0&0\\ 0&1&0&0&0&0&0&0&\bar{\zeta}&\bar{\xi}&0&0&0&0&0\\ 0&0&1&0&0&0&0&0&0&0&\bar{\xi}&\bar{\eta}&0&0&0\\ 0&0&0&1&0&0&0&0&0&0&0&0&\bar{\zeta}&0&0\\ 0&0&0&0&1&0&0&0&0&0&0&0&0&\bar{\xi}&0\\ 0&0&0&0&0&1&0&0&0&0&0&0&0&0&\bar{\eta} \end{array}\right] \left[\begin{array}{c} \beta_1\\ \beta_2\\ \vdots\\ \beta_{15} \end{array}\right], \tag{58b}$$

where $(\bullet)_v$ denotes a vector notation of the corresponding tensor quantity. Compared to the modes given in the work,[18] (58b) does not include the bilinear stress modes which are of subordinate importance and incompatible as pointed out in aforementioned reference. The major advantage of skipping the higher order stress modes is that it allows to straightforwardly construct the L_2-orthogonal enhanced strain field given in (37). Thus, Condition C3 can be fulfilled without tedious orthogonalization procedure. Furthermore, (58) still includes the patch-test (β_1 to β_6), bending (β_7 to β_{12}) and torsion modes (β_{13} to β_{15}) crucial for many engineering problems (see Jabareen and Rubin[76]).

Fortunately, element H1U/h12 fulfills all three design Conditions C1 to C3 for the 15 modes (58) in linear elasticity without further modification. This can be concluded from the fact that the linearization of H1U/h12 coincides with the element proposed by Pfefferkorn and Betsch[18] (see Section 4.4) and the fact that the latter element is specifically designed to fulfill the design conditions for (58). Thus, H1U/h12 is exact for (58) in linear elasticity.

4.5.2 | Nonlinear problems

Unfortunately, it is hardly possible to find similar design conditions and analytic modes in the nonlinear case due to several reasons. First, analytic solutions for nonlinear higher order displacement modes scarcely exist. In special cases

where analytic solutions can be found as, for example, for a bending problem (see Ogden[71] Chapter 5.2.4) the solutions are intricate and include non-polynomial functions. However, using such non-polynomial functions for ansatz spaces is no good idea since this prohibits construction of complete spaces. Moreover, due to the Gauss quadrature, there is, for example, no difference between a suitable cosine function and the corresponding quadratic polynomial ansatz. This means that using such a function has no effect unless undesirable higher order numerical integration is employed. The second difficulty in finding analytic modes for nonlinear problems concerns the plethora of different material models. Even in case of hyperelasticity many models exist[77] which makes it almost impossible to fulfill the design conditions for arbitrary material models.

Therefore, we consider a different approach in the present work:

- The element is designed such that it is exact for the rigid body and patch test modes (i.e., β_1–β_6 in (58)) *regardless* of magnitude of the deformation. This is a standard requirement[‖] for finite elements and corresponding proofs for H1U/h12 are given in Sections 4.2 and 4.6, respectively.
- For the bending and torsion modes (i.e., β_7–β_{15} in (58)) exact solutions for the full nonlinear problem are in general not possible due to the reasons listed above. Instead we chose to fulfill the design Conditions C1 to C3 for these modes only for small (linearized) deformations. Fortunately, in view of the linearization in Section 4.5.1 H1U/h12 automatically meets this relaxed form of the design condition for nonlinear bending and torsion modes. Therefore, even though we cannot expect exact solutions in large deformation problems, results will still be improved compared to the standard Bubnov–Galerkin approach, at least for small deformations. In fact, the numerical results in Sections 5.2 to 5.4 show that the accuracy is greatly increased even for highly nonlinear bending.

4.6 | Patch test

In this section, we show that H1U/h12 passes the patch test, that is, it is capable of correctly representing states of constant stress. This is an important requirement for any finite element and ensures, among other things, convergence with mesh refinement.[81] We consider a homogeneous deformation $\boldsymbol{\varphi}_{\text{ho}} = \mathbf{F}_{\text{ho}}\mathbf{X} + \mathbf{c}_{\text{ho}}$ with constant deformation gradient $\nabla_{\mathbf{X}}\boldsymbol{\varphi} = \mathbf{F}_{\text{ho}}$ and constant vector $\mathbf{c}_{\text{ho}}$. To prove satisfaction of the patch test we now show that $\boldsymbol{\varphi}^{\text{h},e} = \boldsymbol{\varphi}_{\text{ho}}$ is a solution[**] of the numeric problem (15).

First, we obtain from the homogeneous deformation $\boldsymbol{\varphi}^{\text{h},e} = \boldsymbol{\varphi}_{\text{ho}}$, (28) and (23) that $\mathbf{F}_{\varphi}^{\text{h},e} = \mathbf{F}_0 = \mathbf{F}_{\text{ho}}$ since the ansatz for the trial function of the deformations (24) includes complete linear polynomials in the physical space. This follows from the affine map (17) and (25). Second, the non-constant[††] fields (33) and (34) imply $\tilde{\mathbf{h}}^{\text{h},e} = \mathbf{0}$. Consequently, (39) and (6) determine

$$\mathbf{F}^{\text{h},e} = \mathbf{F}_{\text{ho}} \qquad \Rightarrow \qquad \hat{\boldsymbol{\tau}}(\mathbf{F}^{\text{h},e}) = \hat{\boldsymbol{\tau}}_{\text{ho}}, \tag{59}$$

where $\hat{\boldsymbol{\tau}}_{\text{ho}}$ is the constant Kirchhoff stress corresponding to $\mathbf{F}_{\text{ho}}$. These results in combination with the approximations (35) and (36) allow to recast the second equation of the weak form (15b) in the form

$$\int_{\Omega_0^e} \frac{1}{j^{\text{h},e}} \mathbf{F}_0 \mathbf{J}_0^{-\text{T}} \delta\hat{\mathbf{h}}^{\text{h},e} \mathbf{J}_0^{-1} \mathbf{F}_0 j^{\text{h},e} \,\text{d}\hat{\Omega} = \mathbf{0} \qquad \Leftrightarrow \qquad \int_{\hat{\Omega}} \delta\hat{\mathbf{h}}^{\text{h},e} \,\text{d}\hat{\Omega} = \mathbf{0}, \tag{60}$$

which is satisfied exactly by (37). Moreover, with the first Piola Kirchhoff stress tensor $\hat{\mathbf{P}}_{\text{ho}} = \hat{\boldsymbol{\tau}}_{\text{ho}}\mathbf{F}_{\text{ho}}^{-\text{T}}$ the first equation of the weak form (15a) can be written as

$$\int_{\mathcal{B}_0^{\text{h}}} \tilde{\nabla}_{\mathbf{x}}^{\text{s}} \delta\boldsymbol{\varphi}^{\text{h}} : \hat{\boldsymbol{\tau}}_{\text{ho}} \,\text{d}V + G_{\text{ext}}^{\text{h}}(\delta\boldsymbol{\varphi}^{\text{h}}) = 0 \quad \Leftrightarrow \quad \int_{\mathcal{B}_0^{\text{h}}} \nabla_{\mathbf{X}} \delta\boldsymbol{\varphi}^{\text{h}} : \mathbf{P}_{\text{ho}} \,\text{d}V + G_{\text{ext}}^{\text{h}}(\delta\boldsymbol{\varphi}^{\text{h}}) = 0, \tag{61}$$

which is the same as for a isoparametric displacement-based finite element well-known to pass the patch test.[81] Thus, H1U/h12 fulfills the patch test since both equations of (15) are exactly satisfied for $\boldsymbol{\varphi}^{\text{h},e} = \boldsymbol{\varphi}_{\text{ho}}$. This result is confirmed numerically in Section 5.1.1.

4.7 | L_2-orthogonal discrete stress

As usual for EAS elements the discrete independent stresses $\delta\boldsymbol{\tau}^{\mathrm{h},e} \in \mathcal{S}^{\mathrm{h}}$ and $\boldsymbol{\tau}^{\mathrm{h},e} \in \mathcal{T}^{\mathrm{h}}$ have been eliminated from the weak form in Section 2.3.2 via *assumed* L_2-orthogonality between the stress and enhanced strain field. In this section, we present suitable ansatz spaces for the stress which actually fulfill the assumed orthogonality. These functions enable variationally consistent stress recovery during post processing and play a crucial role in Sections 4.8 and 4.9. Suitable stress approximations are given by

$$\delta\boldsymbol{\tau}^{\mathrm{h},e} = \frac{1}{j^{\mathrm{h},e}}\mathbf{F}_0\mathbf{J}_0\delta\overline{\boldsymbol{\tau}}^{\mathrm{h},e}\mathbf{J}_0^{\mathrm{T}}\mathbf{F}_0^{\mathrm{T}} \quad \in \mathcal{S}^{\mathrm{h}}, \tag{62a}$$

$$\boldsymbol{\tau}^{\mathrm{h},e} = \mathbf{F}_0^{-\mathrm{T}}\mathbf{J}_0\overline{\boldsymbol{\tau}}^{\mathrm{h},e}\mathbf{J}_0^{\mathrm{T}}\mathbf{F}_0^{-1} \quad \in \mathcal{T}^{\mathrm{h}}, \tag{62b}$$

where $j^{\mathrm{h},e} = \det(\mathbf{J}^{\mathrm{h},e})$ and $\mathbf{F}_0, \mathbf{J}_0$ are given in (23) and (18), respectively. By choosing $\overline{\boldsymbol{\tau}}^{\mathrm{h},e} = \overline{\boldsymbol{\sigma}}^{*}$ given in (58) the independent stress $\boldsymbol{\tau}^{\mathrm{h},e}$ can immediately be eliminated from (12b). This can easily be verified with (62b), (35), (36) and the fact that

$$\int_{\Omega_0^e} \delta\tilde{\mathbf{h}}^{\mathrm{h},e} : \boldsymbol{\tau}^{\mathrm{h},e}\mathrm{d}V = \int_{\hat{\Omega}} \delta\hat{\mathbf{h}}^{\mathrm{h},e} : \overline{\boldsymbol{\sigma}}^{*}\mathrm{d}\hat{\Omega} = 0 \tag{63}$$

holds regardless of element geometry as consequence of the particular choice (36) (see also the design Condition C3 in Section 4.5.1). A similar procedure can also be applied for the test function of the independent stress in (12c). Here we choose $\delta\overline{\boldsymbol{\tau}}^{\mathrm{h},e} = \delta\overline{\boldsymbol{\sigma}}^{*}$ where $\delta\overline{\boldsymbol{\sigma}}^{*}$ has the same form as $\overline{\boldsymbol{\sigma}}^{*}$ given in (58) but uses the isoparametric coordinates $\boldsymbol{\xi}$ instead of the skew $\bar{\boldsymbol{\xi}}$. Unfortunately, the resulting $\delta\boldsymbol{\tau}^{\mathrm{h},e}$ is only automatically L_2-orthogonal to $\tilde{\mathbf{h}}^{\mathrm{h},e}$ given in (31) in case of regular meshes[‡‡]. However, for distorted geometries a Gram–Schmidt orthogonalization procedure similar to the one proposed by Pfefferkorn and Betsch[18] allows to straightforwardly construct an orthogonal $\delta\boldsymbol{\tau}^{\mathrm{h},e}$ field. Thus, the test function $\delta\boldsymbol{\tau}^{\mathrm{h},e}$ can always be eliminated from (12c) which concludes the proof that suitable L_2-orthogonal stress approximations exist.

4.8 | L_2-orthogonality to constant pressure

Nagtegaal and Fox[65] proposed the *ad hoc* condition that small changes of the enhanced field may not contribute to volume changes. They suggest that this condition should be added to the standard requirements on enhanced fields since they suppose it improves stability of EAS elements. Alternatively, the volume condition can also be obtained by requiring that the test function for the enhanced field is L_2-orthogonal to a *piecewise constant pressure field*.[64,65] We substantiate the claim of increased stability and discuss its connection to the L_2-orthogonality to a piecewise constant pressure field in Section 4.9.

Here, we present, motivated by the discussion in Section 4.9, a slightly modified version of the condition proposed by Nagtegaal and Fox[65]. Instead of requiring orthogonality to a piecewise constant *constitutive* pressure field we consider L_2-orthogonality between the enhanced fields $\delta\tilde{\mathbf{h}}^{\mathrm{h},e}$, $\tilde{\mathbf{h}}^{\mathrm{h},e}$ and *independent* Kirchhoff stress[64] of the form $\delta\boldsymbol{\tau}_p^{\mathrm{h},e} = (j^{\mathrm{h},e})^{-1}\delta p_0^{\mathrm{h},e}\mathbf{I}$ and $\boldsymbol{\tau}_p^{\mathrm{h},e} = p_0^{\mathrm{h},e}\mathbf{I}$ where $\delta p_0^{\mathrm{h},e}, p_0^{\mathrm{h},e}$ are piecewise (elementwise) constant[§§]. The L_2-orthogonality conditions can now be written as

$$\int_{\Omega_0^e} \delta\tilde{\mathbf{h}}^{\mathrm{h},e} : p_0^{\mathrm{h},e}\mathbf{I}\mathrm{d}V = 0, \tag{64a}$$

$$\int_{\Omega_0^e} \frac{1}{j^{\mathrm{h},e}}\delta p_0^{\mathrm{h},e}\mathbf{I} : \tilde{\mathbf{h}}^{\mathrm{h},e}\mathrm{d}V = 0. \tag{64b}$$

Since the stress $\boldsymbol{\tau}_p^{\mathrm{h},e} \in \mathcal{T}^{\mathrm{h}}$ and $\mathcal{T}^{\mathrm{h}}$ includes constant modes (see Section 4.7), condition (64a) is automatically fulfilled due to the L_2-orthogonality described in Section 4.7. Unfortunately, pressure fields $\delta\boldsymbol{\tau}_p^{\mathrm{h},e}$ are in general not part of $\mathcal{S}^{\mathrm{h}}$ due to the orthogonalization procedure required in case of distorted meshes. However, (64b) holds automatically in case of regular meshes and seems to be important at least in this relaxed sense.

Remark 4. For comparison, considering an F-enhanced EAS element, (14) and the transformation $\mathbf{P}_p^{\mathrm{h},e} = \boldsymbol{\tau}_p^{\mathrm{h},e}(\mathbf{F}^{\mathrm{h},e})^{-\mathrm{T}}$ yields

$$\int_{\Omega_0^e} \delta\tilde{\mathbf{F}}^{\mathrm{h},e} : \mathbf{P}_p^{\mathrm{h},e} \mathrm{d}V = 0 \qquad \Leftrightarrow \qquad \int_{\Omega_0^e} \mathrm{tr}\left(\delta\tilde{\mathbf{F}}^{\mathrm{h},e}(\mathbf{F}^{\mathrm{h},e})^{-1}\right) \mathrm{d}V = 0 \tag{65a}$$

instead of (64a). This is a nonlinear condition which cannot easily be fulfilled for arbitrary deformation gradients $\mathbf{F}^{\mathrm{h},e}$.[65] A possibility is choosing $\delta\tilde{\mathbf{F}}^{\mathrm{h},e} = \delta\tilde{\mathbf{h}}^{\mathrm{h},e}\mathbf{F}^{\mathrm{h},e}$ for the test function of the enhanced deformation gradient. Unfortunately, this is not enough to get a stable finite element as our numerical experiments confirmed. Apparently, it would be necessary to simultaneously fulfill

$$\int_{\Omega_0^e} \delta\boldsymbol{\tau}_p^{\mathrm{h},e}(\mathbf{F}^{\mathrm{h},e})^{-\mathrm{T}} : \tilde{\mathbf{F}}^{\mathrm{h},e} \mathrm{d}V = 0 \qquad \Leftrightarrow \qquad \int_{\Omega_0^e} \mathrm{tr}\left(\tilde{\mathbf{F}}^{\mathrm{h},e}(\mathbf{F}^{\mathrm{h},e})^{-1}\right) \mathrm{d}V = 0 \tag{65b}$$

at least for regular meshes. The last equation corresponds to (64b) and in contrast to (65a) it seems hardly possible to find suitable ansatz functions for $\tilde{\mathbf{F}}^{\mathrm{h},e}$ such that (65b) is satisfied for all $\mathbf{F}^{\mathrm{h},e}$ since both $\tilde{\mathbf{F}}^{\mathrm{h},e}$ and $\mathbf{F}^{\mathrm{h},e}$ depend on $\tilde{\mathbf{F}}^{\mathrm{h},e}$.

4.9 | Stability

The last but not least property of the novel finite element we discuss is its stability. In particular we are concerned with *hourglassing-instabilities* from which almost all EAS elements suffer. To the best knowledge of the authors the only exemption is the element for explicit dynamics proposed in the PhD-thesis of Schmied[64] which is based on h-enhancement similarly to H1U/h12.

The numerical investigations in Section 5 (especially Sections 5.6 to 5.9) cover many cases in which other EAS elements and mixed approaches famously exhibit hourglassing instabilities. The newly proposed element H1U/h12 passes all these tests without any problems which strongly suggests its improved stability. Yet, it is of course no mathematically sound proof which is beyond the scope of the present contribution. However, we suggest:

Hypothesis 1. *Satisfaction of the piecewise constant pressure orthogonality conditions (64) is a necessary condition for stability.*

We back our claim by recalling that in the very first publication on geometrically linear EAS elements Simo and Rifai[1] already observed spurious oscillations of the variationally consistent pressure field. Later, Reddy and Simo[82] provided a mathematical proof revealing that the independent stress field of EAS elements exhibits *checkerboard modes* similar to the Q1/P0 element. These instable modes exist due to a violation of the inf-sup condition which is thoroughly covered by Boffi et al.[83] and for EAS elements in References 82,84. Fortunately, in case of the standard linear elastic EAS element,[1] the checkerboard modes are confined to the independent stress. The displacements as well as the enhanced strains are unaffected (see Lamichane et al.[84] and Djoko et al.[85]). Thus, by either employing L_2-smoothing of the independent stress[1] or by using the constitutive stress for post-processed results, the instable checkerboard modes do not affect linear EAS elements in practical simulations.

Returning now to nonlinear EAS elements we observe from (65) that the enhanced field is coupled with piecewise constant pressure (checkerboard modes) in case of F-enhancement. Our suggestion is that this leads to instabilities from the independent stress field being transferred to the enhanced field and ultimately the well-known hourglassing first observed by Wriggers and Reese.[46] The coupling between enhanced fields and checkerboard modes can be avoided with h-enhancement since it is simple to satisfy (64). In particular, H1U/h12 fulfills (64) at least for regular meshes. Thus, the enhanced field is decoupled from *independent* constant pressure and instabilities *cannot* be transmitted from the stress to the strain field. We believe that this explains the *increased stability* of H1U/h12.

Remark 5. Unfortunately, satisfaction of Hypothesis 1 is not sufficient. For example, if $\mathbf{F}^{\mathrm{h},e}$ is used instead of $\mathbf{F}_0$ in (22) we observe instabilities (only) for *rectangular* element shapes in the one element stability analysis (see Section 5.6) even though the element still satisfies (64).

5 | NUMERICAL INVESTIGATIONS

This section covers extensive numerical studies to assess the performance of the newly proposed element **H1U/h12** (Q1U/h4)[¶¶] and compare it to existing elements. The numerical examples cover a wide range of features including mesh distortion sensitivity, robustness and stability in hyperelastic as well as elasto-plastic simulations. Focus is put on three-dimensional hexahedral elements. However, results can at least qualitatively be transferred to two-dimensional plane-strain problems if not mentioned otherwise.

5.1 | Element types

The (standard) Bubnov–Galerkin finite elements used in our numerical investigations for comparison with H1U/h12 are:

- **H1/E9** (Q1/E4): Standard EAS element by Simo and Armero[2] with the classical nine (four in 2D) Wilson-modes and F-enhancement.
- **HA1/E12T** (QA1/E4T): Standard EAS element using the transposed Wilson-modes to avoid the instability under compression and three additional volumetric enhanced modes. Additionally, a modification of the gradient of the compatible shape functions and a special nine point (five in 2D) Gauss quadrature rule are used. The element is implemented as described by Pfefferkorn and Betsch[16] and closely related to the improved EAS version by Simo et al.[5]
- **H1/P0** (Q1/P0): Mixed pressure element by Simo et al.[80] based on a Hu–Washizu functional with elementwise constant pressure field.
- **H1/P0E6T** (Q1/P0E2T): Combination of H1/P0 and H1/E9T which was proposed by Armero[54] for 2D plane strain problems (Q1/P0E2T). A 3D extension (H1/P0E6T) has recently been proposed by Hille et al.[59]
- **H1/S18** (Q1/S5): Assumed stress element as proposed by Pian and Sumihara[74] and Pian and Tong[86] for linear elasticity in 2D and 3D, respectively. An extension to nonlinear problems can, for example, be found in the work of Viebahn et al.[29] However, we use the inverse stress strain relation for a Neo-Hookean material model proposed by Pfefferkorn et al.[19] instead of the numeric procedure in aforementioned reference.

We also consider other *Petrov–Galerkin enhanced assumed strain (PG-EAS)* elements in addition to H1U/h12. All of which use the same set of ansatz functions (see Section 3.2) and differ only in the type of enhancement and required transformations for objectivity. In particular we investigate:

- **H1U/E12** (Q1U/E4): E-enhancement (see Section 3.3.3).
- **H1U/F12** (Q1U/F4) and **H1U/F12T** (Q1U/E4T): F-enhancement as described in Section 2.3, Remark 3 and Section 3.3.2. H1U/F12T uses the transposed Wilson-modes (i.e., the transpose of (33)) only for the trial function of the enhancement.

5.2 | Material models

For the *hyperelastic* simulations we consider a Neo-Hookean (NH) and Ogden (OG) material. The former is chosen as standard material model and the latter allows to deliberately construct a material with an instability under tension. Such instabilities induce hourglassing for some elements which is thoroughly covered in Sections 5.6 and 5.7. The strain-energy functions of the two hyperelastic material models are given by

$$W_{\mathrm{NH}} = \frac{\mu}{2}\left(\mathrm{tr}(\mathbf{F}^{\mathrm{T}}\mathbf{F}) - 3\right) + \frac{\lambda}{2}\ln^2(J) - \mu\ln(J), \tag{66a}$$

$$W_{\mathrm{OG}} = \sum_{j=1}^{n_p}\sum_{i=1}^{3}\frac{\mu_p}{\alpha_p}\left(\overline{\lambda}_i^{\alpha_p} - 1\right) + \kappa\beta^{-2}\left(\beta\ln(J) + J^{-\beta} - 1\right), \tag{66b}$$

where $J = \det\mathbf{F}$ is the determinant of the deformation gradient (39) and $\overline{\lambda}_i = J^{-\frac{1}{3}}\lambda_i, i = 1, 2, 3$ are the deviatoric parts of the principal stretches λ_i. Furthermore, λ, μ, and κ are the two Lamé-constants and the bulk modulus and β, α_p, μ_p, n_p

TABLE 1 Overview of the material models employed for the various benchmarks.

Benchmark	Section	Material models
Patch test	5.1.1	NH, EP
Frame invariance	5.1.2	NH
Objectivity	5.1.3	NH, EP
Eigenvalues	5.1.4	NH
Mesh distortion	5.2	NH
Roll-up	5.3	NH
Cook's membrane	5.4	NH
Thin circular ring	5.5	NH
One element stability	5.6	OG
Large mesh stability	5.7	OG
Necking plane strain	5.8	EP
Necking circular bar	5.9	EP

Note: Neo-Hookean (NH), Ogden (OG), and elasto-plastic (EP) material model.

are further material constants specified in the respective examples. The eigenvalue decomposition required for the Ogden material is carried out using a numerical eigenvalue and eigenvector computation and proper treatment of duplicate eigenvalues for the material tangent (see e.g., References 73,87).

In addition to the hyperelastic material, we consider the eigenvalue based *elasto-plastic* (EP) material model proposed by Simo.[88] It contains the multiplicative elasto-plastic split, nonlinear isotropic hardening, the von Mises yield condition and a Hencky elastic law. The same eigenvalue routine as described for the Ogden model is used. This material is a standard model in finite element technology[5,17,54,66] and employed with the standard material parameters $\mu = 80.1938$, $\kappa = 164.206$, $\sigma_{Y0} = 0.45$, $\sigma_{Y\infty} = 0.715$, $\delta = 16.93$, and $H = 0.12924$.[1,2,5,10,14,17,54,88,89] For all elasto-plastic simulations we use the *line-search* algorithm described by Bonet and Wood[87] to stabilize the Newton–Raphson scheme. Hyperelastic simulations do *not* employ the line-search algorithm.

Table 1 gives an overview of the material models used for the numerical examples in this section.

5.3 | Stress recovery

All stress results shown in the present work are computed using a L_2-smoothing procedure to project the stress from the Gauss points to the nodes. It is given by

$$\sum_{e=1}^{n_{\text{el}}} \tau_i \int_{\Omega^e} N_i N_j \mathrm{d}V \sigma_j = \sum_{e=1}^{n_{\text{el}}} \tau_i \int_{\Omega^e} N_i \hat{\sigma} \mathrm{d}V, \qquad \forall \tau_i \in \mathbb{R}, \tag{67}$$

where N_i are the standard Lagrangian shape functions, σ_j the stress at node j and $\hat{\sigma}$ the constitutive stress (for H1/S18 we use the independent stress). Usually, we plot results for the von Mises stress. However, (67) can be used for any stress component.

5.4 | Basic tests

In this section, we briefly summarize results of some fundamental numerical tests for H1U/h12. Full descriptions of the tests' setup and thresholds to verify if the test is passed can be found in the references mentioned below.

5.4.1 | Patch test

We conduct the numerical patch test exactly as described by Pfefferkorn and Betsch.[16-18] Element H1U/h12 passes the test for elastic and elasto-plastic material as expected from the analytic investigation in Section 4.6. See Figure 2 for a stress plot computed with the novel finite element.

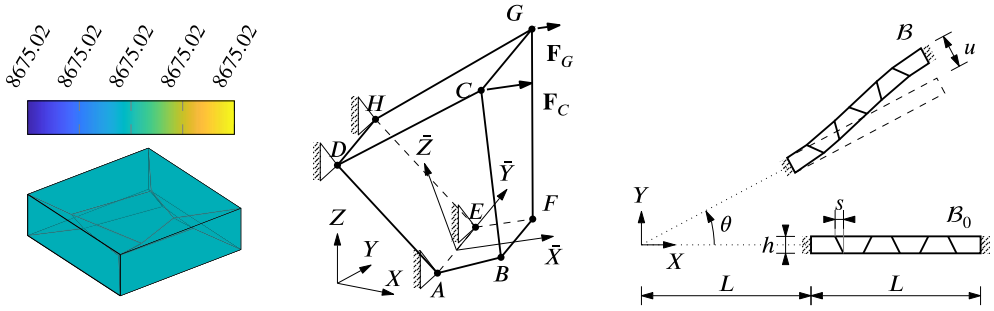

FIGURE 2 Von Mises stress distribution for the patch test with distorted mesh (left). Geometry and boundary conditions for the isotropy and invariance test (middle) and the objectivity test (right).

5.4.2 | Frame invariance and isotropy

H1U/h12 also passes the frame invariance and isotropy benchmark which is fully described in the work of Pfefferkorn and Betsch.[18] Figure 2 shows the single finite element used to check the two properties. Corresponding analytic proofs that the element passes this numerical test are presented in Sections 4.2 and 4.3.

5.4.3 | Objectivity

Another basic test concerns the objectivity of H1U/h12 which is investigated by examining the effect of superimposed rigid body motions on a beam-like structure (see Figure 2). A full description of the test is given in Reference 17. The only difference in this work is the use of distorted elements ($s = h/2$) as shown in Figure 2 to ensure that the metric ansatz functions do not coincide with the standard ansatz functions. Furthermore, as described by Pfefferkorn and Betsch,[17] the test also covers path independence. Again, element H1U/h12 passes both tests for elastic and plastic materials which is inline with Sections 4.2 and 4.3.

5.4.4 | Eigenvalue analysis

A final simple numerical benchmark concerns the eigenvalue analysis of a single (regular or distorted) finite element in the reference configuration which can be used to determine whether or not the element is prone to volumetric locking. Refer to Pfefferkorn and Betsch[16-18] for a full description of this benchmark. In this test H1U/h12 exhibits the correct distribution of eigenvalues with only one "locking" mode regardless of mesh distortion. However, as analogously discovered for the corresponding linear elastic element,[18] H1U/h12 exhibits two eigenvalue pairs with non-negligible complex part. Fortunately, this does not seem to have negative effects on the elements performance as our extensive numerical studies show.

5.5 | Mesh distortion test

The first benchmark for features beyond basic requirements concerns mesh distortion sensitivity. To that end we consider a 3D version[16,18] of the standard 2D test.[1,12,14,22,49,90,91] The beam like structure shown in Figure 3 has the dimensions $l \times b \times h = 10 \times 1 \times 2$ and is meshed with only two elements. Distortion is applied on two nodes via parameter s as shown in Figure 3. Fixed boundary conditions $u(X = 0, Y, Z) = 0$, $v(X = 0, Y = 0, Z) = 0$ and $w(X = 0, Y, Z = 0) = 0$ apply on the left end ($X = 0$) while the other end is subjected to a bending moment $M = 20$ applied in the form of a traction boundary condition. It is given by $\sigma(Z) = 30\,(1 - Z)$ and modeled as dead load. We choose the Neo-Hookean material model with parameters $\mu = 600$ and $\lambda = 600$ for this test which corresponds to $E = 1500$ and $\nu = 0.25$.

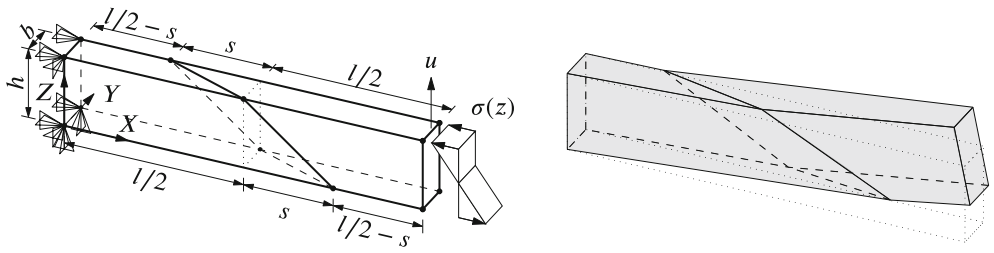

FIGURE 3 Mesh distortion test. Setup (left) and deformed configuration for $s = 3$ (right). Deformed configuration computed with H1U/h12.

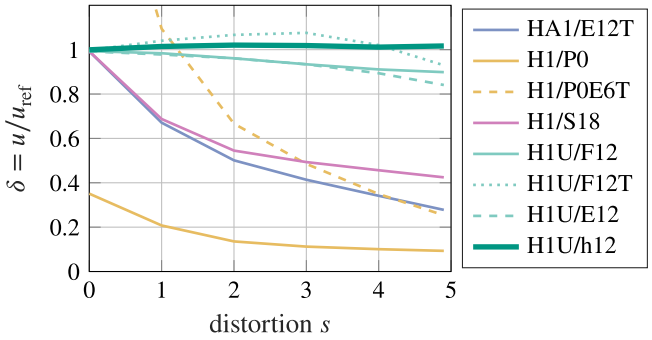

FIGURE 4 Results of the mesh distortion test. Normalized top edge displacement δ plotted over distortion s.

The setup is chosen such, that the analytic solution in linear elasticity is $u = 1$.[76] However, for the nonlinear problem we use $u_{\text{ref}} = 0.96897$ computed with a fine regular mesh of $40 \times 8 \times 4$ HA1/E12 elements as reference solution. Displacement u denotes the mean value of the displacement in Z-direction of the two nodes at the top edge on the right face (see Figure 3) which is normalized with u_{ref}. Figure 4 shows the resulting $\delta = u/u_{\text{ref}}$ for several elements.

Element H1/S18 exhibits the best performance of the standard elements with almost the correct displacement ($|\delta - 1| < 1\%$) for no distortion and the least deterioration with mesh distortion. H1/P0E6T behaves far too soft in case of no distortion. In fact there is a "optimal" distortion for which the element is exact, which explains the great performance of that element in the Cook's membrane example in Section 5.4.

The novel PG-EAS elements perform far better than any of the standard elements. After all, they are specifically crafted to be exact in linear elastic bending problems (see Section 4.5) which also greatly improves their accuracy in this nonlinear test. However, results are not as accurate as in the linear elastic case and there are, as expected (see Section 4.5.2), small deviations from the optimal result $\delta = 1$. Of the tested PG-EAS elements the newly proposed H1U/h12 is the most accurate with $|\delta - 1| < 2.1\%$ for all distortions. The other PG-EAS elements are slightly less accurate but still outperform all standard Bubnov-Galerkin finite elements.

Remark 6. Interestingly, none of the PG-EAS elements converges in the Newton–Raphson scheme regardless of number of load steps for the two special meshes proposed by Pfefferkorn and Betsch.[18] There seems to be some sort of instability which might be associated with horizontal displacements observed due to the combination of non-symmetric Dirichlet boundary conditions and mesh distortion. If either a regular or finer mesh is considered, the solution converges as usual.

5.6 | Roll-up

Our next example concerns the classical roll-up of a beam to show that the novel approach also improves the element's behavior in distorted meshes for considerable bending. Similar to the previous example we study a beam-like structure with dimensions $L = 10$, $b = 2$, and $t = 0.5$ which is subjected to a bending moment

$$M = \frac{2\pi EI}{L}\left(1 - \frac{2}{3}\frac{\pi^2 t^2}{L^2}\right), \qquad I = \frac{bt^3}{12} \tag{68}$$

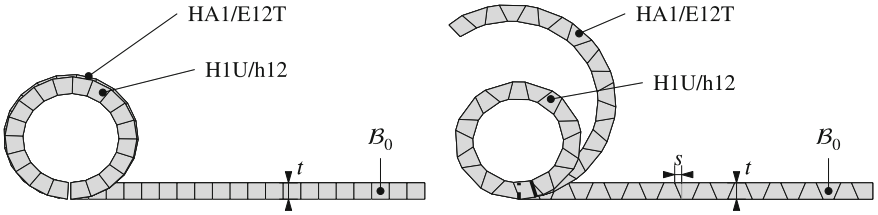

FIGURE 5 Roll-up of a beam. Reference $\mathcal{B}_0$ and deformed configuration for HA1/E12T and H1U/h12 for a regular (left) and distorted (right) mesh. Thick dashed and solid line show beginning and end of the beam with H1U/h12 and the distorted mesh (right).

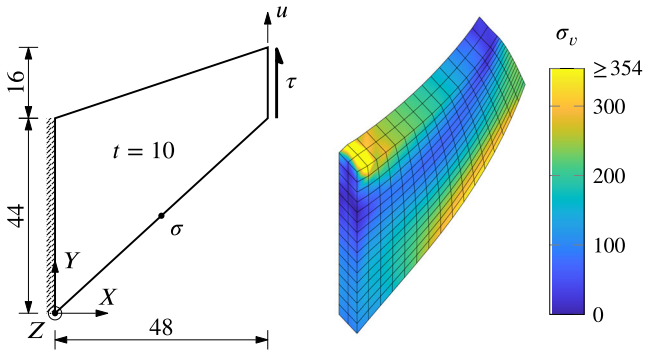

FIGURE 6 Setup of the Cook's membrane test (left) and deformed configuration with von Mises stress distribution computed with $16 \times 16 \times 2$ H1U/h12 elements (right). The colors are capped at $0.65\sigma_{v,\max} = 354$ to avoid domination of the stress singularity in the plot.

applied on the right end in the form of a linearly distributed follower load. Thus, it stays normal to the deformed surface and is scaled with the deformed area (see e.g., Wriggers[69] Ch. 4.2.5). The moment (68) is taken from the work of Müller and Bischoff[92] and accounts for the rather thick beam in contrast to the usually used $M = 2\pi EI/L$ which is only valid for thin beams. Dirichlet boundary conditions $u(X = 0, Y, Z) = 0$, $v(X = 0, Y = 0, Z) = 0$ and $w(X = 0, Y, Z = 0) = 0$ apply on the left end and we consider a regular and distorted mesh with 20 elements as shown in Figure 5. The material parameters of the Neo-Hookean model are chosen to $\mu = 500$ and $\lambda = 0$ which correspond to $E = 1000$ and $\nu = 0$.

Figure 5 shows the final configuration computed with HA1/E12T and H1U/h12. The former is only capable of (almost) correctly depicting the roll-up into a circular shape in case of a regular mesh and is well off the desired shape in case of distortion. However, the newly proposed H1U/h12 is able to give good results for both meshes with only slightly too soft behavior due to the distortion. Thus, it can be concluded, that the Petrov–Galerkin approach improves performance not only for "moderate" bending (see Section 5.2) but also in case of much larger curvatures.

5.7 | Cook's membrane

The classical Cook's membrane example[1,2,4,10,16-18,54,57,58] covers convergence of displacements and stresses with mesh refinement as well as coarse mesh accuracy. Figure 6 shows the tapered trapezoidal specimen which is clamped on the left side ($\mathbf{u}(X = 0, Y, Z) = \mathbf{0}$) and subjected to a constant shear force $\tau = 100$ in y-direction. Again, we use the Neo-Hookean material with the parameters chosen to $\lambda = 8.2669 \cdot 10^4$ and $\mu = 756.00$ (corresponding to a nearly incompressible material with $E = 2261.2$ and $\nu = 0.4955$). A mesh with two elements in direction of thickness and $n_{el} = \{2, 4, 8, 16\}$ elements in the other two directions completes the setup.

Figure 7 shows the displacement u of the top right corner in Y-direction and the stress σ at the midpoint of the lower surface (see Figure 6) for increasingly fine meshes. H1/P0E6T exhibits seemingly the best results of the standard elements. However, as shown in Section 5.2 it is too soft in bending dominated problems with moderate distortion. Thus, the good results of H1/P0E6T in this test are due to the "correct distortion" of the mesh. H1/S18 is the next best standard element and shows especially fast stress convergence which even competes with the results of the Petrov–Galerkin finite elements.

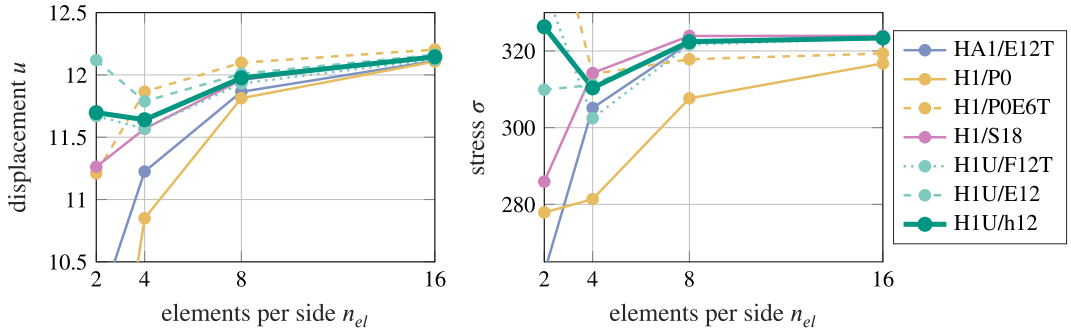

FIGURE 7 Results of the Cook's membrane benchmark. Convergence of the displacement u (left) and stress σ (right) with mesh refinement.

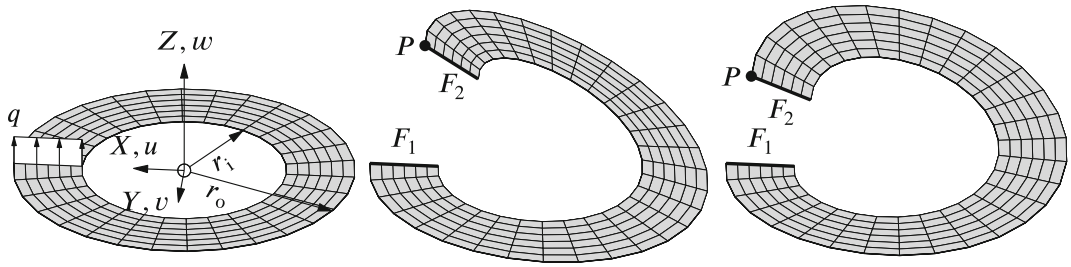

FIGURE 8 Geometry for thin circular ring (left) and deformed configuration computed with $2 \times 6 \times 30$ H1/S18 (middle) and H1U/h12 (right) elements.

All unsymmetric elements exhibit fairly similar results with an odd kink for very coarse meshes. The novel H1U/h12 exhibits fast convergence of the displacements and only marginally slower convergence of the stresses in comparison to H1/S18. All in all, the newly proposed element gives accurate results in this test as well.

5.8 | Thin circular ring

In this section, we conduct the *thin circular ring* example[14,19,93] shown in Figure 8 to examine the element's robustness in the Newton–Raphson scheme. We characterize robustness by the size of applicable load steps and number of Newton–Raphson iterations required for convergence.[19] Robustness is naturally highly influenced by the settings for the Newton–Raphson scheme. We choose a convergence criterion based on the norm of the residual $||\mathbf{R}|| < 10^{-8}$ and assert failure of the Newton–Raphson scheme if either $||\mathbf{R}|| > 10^{14}$ or more than 20 iterations are necessary for convergence within one load step. Figure 8 shows the slit circular ring with dimensions $r_i = 6$, $r_o = 10$ and $t = 0.03$. Boundary conditions $u(0, 0, 0) = 0$, $v(X, Z, Y = 0) = 0$ and $w(X, Y = 0, Z = 0) = 0$ apply at face F_1 and face F_2 is subjected to a dead load $q = 6.67$ in Z-direction. To complete the setup, we consider the Neo-Hookean material model with $\mu = 10.5 \cdot 10^3$ and $\lambda = 0$.

The converged displacement w_P of point P in Z-direction computed with a very fine mesh with $8 \times 24 \times 120$ elements is $w_P \approx 10.265$ for both H1/S18 and H1U/h12. However, Figure 8 shows the deformed configuration for the coarser mesh with $2 \times 6 \times 30$ elements for H1/S18 with $w_P = 9.741$ and H1U/h12 with $w_P = 7.978$, respectively. Therefore, both behave too stiff and the different displacements make comparison regarding robustness difficult. In order to get a "fair" comparison of the element's robustness we only consider a mesh with $4 \times 12 \times 60$ elements for which the displacements w_P (see Table 2) are similar.

Table 2 also lists the required number of load steps n_{steps} and total number of Newton–Raphson iterations n_{NR} for various element types. H1/S18 exhibits the most favorable behavior with only one required load step and seven Newton–Raphson iterations. This is inline with the results of Magisano et al.[28] and Pfefferkorn et al.[19] who observed the high robustness of assumed stress elements in many examples. All EAS elements require many more load steps

TABLE 2 Results of the thin circular ring test.

Element type	req. n_{steps}	Total n_{NR}	w_{P}
H1/S18	1	7	10.235
HA1/E12T	5	80	9.970
HA1/E12T-MIP	2	14	9.970
H1U/E12	8	106	10.286
H1U/F12	8	107	10.292
H1U/F12T	7	96	10.224
H1U/h12	6	90	10.200
H1U/h12-MIP	2	16	10.200

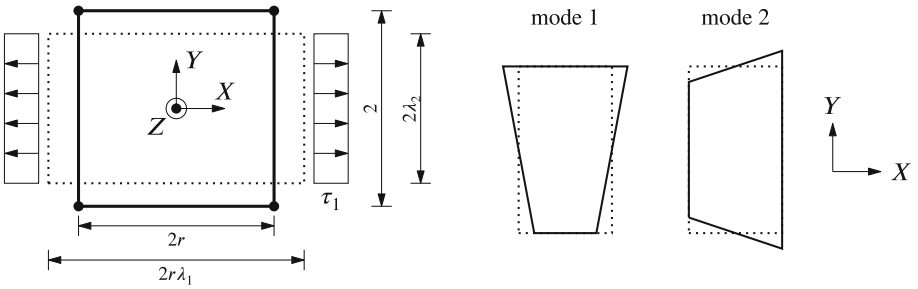

FIGURE 9 Geometry for the stability test (left) and 2D hourglass modes computed for $\lambda_1 = 0.75$ (right, solid line). The deformed state is depicted in both figures with dotted lines.

and iterations. However, this can be greatly improved with the MIP method briefly described in Section 3.4 and introduced for EAS elements by Pfefferkorn et al.[19] For the novel H1U/h12 the MIP method allows to reduce n_{NR} by a factor of ≈ 5.6.

5.9 | One element stability analysis

The next two tests concern the stability of the finite elements and are used to determine if elements are prone to hourglassing. To that end we first consider the unconstrained one element stability test proposed by Glaser and Armero[54] which has recently been extended to 3D problems by Pfefferkorn and Betsch.[17] The advantage of the unconstrained compared to the constrained test proposed by Wriggers and Reese[46] is that it can also be used to examine hourglassing due to material instabilities.

We consider the Ogden material model (66b) with $\beta = 2$, $\kappa = 10^5 + 20/3$, $n_p = 1$, $\alpha_1 = 0.5$, $\mu_1 = 80$ which corresponds to $\mu = 20$ and $\lambda = 10^5$ in linear theory. Note that the material parameters are deliberately chosen such that a material instability under tension occurs at $\lambda_1^{\text{crit}} \approx 3$ and $\lambda_1^{\text{crit}} \approx 1.75$ for the first and second Piola-Kirchhoff stress, respectively.[10] This instability is similar to the one of the elasto-plastic material model which is well-known[10,14,17,54] to trigger hourglassing. However, the Ogden model yields more distinct results which is why it is employed here.

The test is performed on a single element (see Figure 9) with reference configuration $\Omega_0^e = [-r, +r] \times [-1, +1] \times [-1, +1]$ where r governs the element's aspect ratio. Usually, it is not necessary to consider initially rectangular geometries with $r \neq 1$ since Armero[54] showed that different aspect ratios only change when[|||] and not if instabilities occur. However, this is not necessarily true for some of the unsymmetric finite elements which is discussed below.

The homogeneous deformation state shown in Figure 9 is associated with a diagonal deformation gradient of the form $\mathbf{F} = diag([\lambda_1, \lambda_2, \lambda_3])$. Therein, $\lambda_i,\ i = 1, 2, 3$ are the principal stretches associated with the principal axes which coincide with coordinate system shown in Figure 9. Furthermore, choosing a specific λ_1 allows to compute the other principal

stretches from the material model and the boundary conditions. In case of a 2D plane strain problem we have $\lambda_3 = 1$ and λ_2 can be computed from $\tau_2 = 0$. Similarly, in 3D uniaxial tension $\lambda_2 = \lambda_3$ can be determined from $\tau_2 = \tau_3 = 0$.

This analytic solution can then be imposed on the finite element in order to compute the corresponding stiffness matrix $\mathbf{K}^e$ of the element. Furthermore, the hourglass eigenvectors of $\mathbf{K}^e$ arranged row-wise in matrix $\mathbb{P}_{\text{hour}}$ can be determined in closed form for this example. In 2D plane strain they are always given by

$$\mathbb{P}_{\text{hour}} = \frac{1}{4}\begin{bmatrix} 1 & 0 & -1 & 0 & 1 & 0 & -1 & 0 \\ 0 & 1 & 0 & -1 & 0 & 1 & 0 & -1 \end{bmatrix}. \tag{69}$$

Unfortunately, no equivalently simple structure exists for the 3D problem. Nevertheless, it is possible to find the eigenvectors in closed form with the procedure described by Pfefferkorn and Betsch[17] for symmetric elements. Interestingly, the approach can also be used for most of PG-EAS elements since their stiffness matrix is symmetric for the present load state and regular mesh. However, in case of H1U/h12 $\mathbf{K}^e$ looses its symmetry and the method has to be modified. The eigenvectors are then given by[17]

$$\mathbb{P}_{\text{hour}} = \begin{bmatrix} 0 & 0 & 0 & 0 & 0 & 0 & 0 & 0 & 0 & 1 & 0 & 0 \\ 0 & 0 & 0 & 0 & 0 & 0 & 0 & 0 & 0 & 0 & 1 & 0 \\ 0 & 0 & 0 & 0 & 0 & 0 & 0 & 0 & 0 & 0 & 0 & 1 \\ 0 & 0 & 0 & 0 & -1 & 0 & 0 & 0 & 1 & 0 & 0 & 0 \\ 0 & 0 & 0 & 0 & 0 & -1 & 0 & 1 & 0 & 0 & 0 & 0 \\ 0 & 0 & 0 & 0 & 0 & 1 & 0 & 1 & 0 & 0 & 0 & 0 \\ 0 & U_1 & 0 & 1 & 0 & 0 & 0 & 0 & 0 & 0 & 0 & 0 \\ 0 & U_2 & 0 & 1 & 0 & 0 & 0 & 0 & 0 & 0 & 0 & 0 \\ 0 & 0 & U_1 & 0 & 0 & 0 & 1 & 0 & 0 & 0 & 0 & 0 \\ 0 & 0 & U_2 & 0 & 0 & 0 & 1 & 0 & 0 & 0 & 0 & 0 \\ V_1 & 0 & 0 & 0 & 1 & 0 & 0 & 0 & 1 & 0 & 0 & 0 \\ V_2 & 0 & 0 & 0 & 1 & 0 & 0 & 0 & 1 & 0 & 0 & 0 \end{bmatrix} \underbrace{\frac{1}{8}\begin{bmatrix} \mathbf{h}_1 \odot \mathbf{I} \\ \vdots \\ \mathbf{h}_4 \odot \mathbf{I} \end{bmatrix}}_{\mathbb{H}_{\text{hour}}}, \tag{70}$$

where $\mathbf{I}$ is the identity matrix, $\mathbf{h}_i$ are the hourglass vectors given in (20c) and "$\odot$" denotes the Kronecker product.[94] Furthermore, U_i and V_i, $i = 1, 2$ can directly be computed from the components of the sparse[17] matrix $\mathbf{k}^e = [k_{ij}] = \mathbb{H}_{\text{hour}}\mathbf{K}^e\mathbb{H}_{\text{hour}}^{\text{T}}$ and are given by

$$U_{1,2} = -\frac{p_1}{2} \pm \sqrt{\frac{p_1^2}{4} + 1}, \qquad p_1 = \frac{k_{44} - k_{22}}{k_{24}}, \tag{71}$$

$$V_{1,2} = -\frac{p_2}{2} \pm \sqrt{\frac{p_2^2}{4} + 2\frac{k_{15}}{k_{51}}}, \qquad p_2 = \frac{k_{55} - k_{11} + k_{59}}{k_{51}}. \tag{72}$$

Thus, the only difference to the method proposed by Pfefferkorn and Betsch[17] is that it considers the *only* unsymmetric entry $k_{15} \neq k_{51}$ of $\mathbf{k}^e$. Figures 9 and 10 show the computed eigenmodes in 3D for $\lambda_1 = 0.75$. Ultimately, the hourglass eigenvectors can be used to evaluate

$$diag([\omega_i^{\text{hour}}]) = (\mathbb{P}^{\text{hour}})^{-\text{T}}\mathbf{K}^e(\mathbb{P}^{\text{hour}})^{\text{T}}, \tag{73}$$

which yields a diagonal matrix[***] with the eigenvalues ω_i^{hour}. If any negative hourglass eigenvalues occur the element is likely to be prone to hourglassing. Whether or not hourglass modes actually occur can then be verified with the simulation described in Section 5.7.

Figure 11 shows the hourglass eigenvalues ω_i^{hour} for several 2D elements in dependence of λ_1. The F-enhanced PG-EAS Q1U/F4 and Q1U/E4 both coincide with Q1/S5 and are therefore not included in the plots. These three elements all

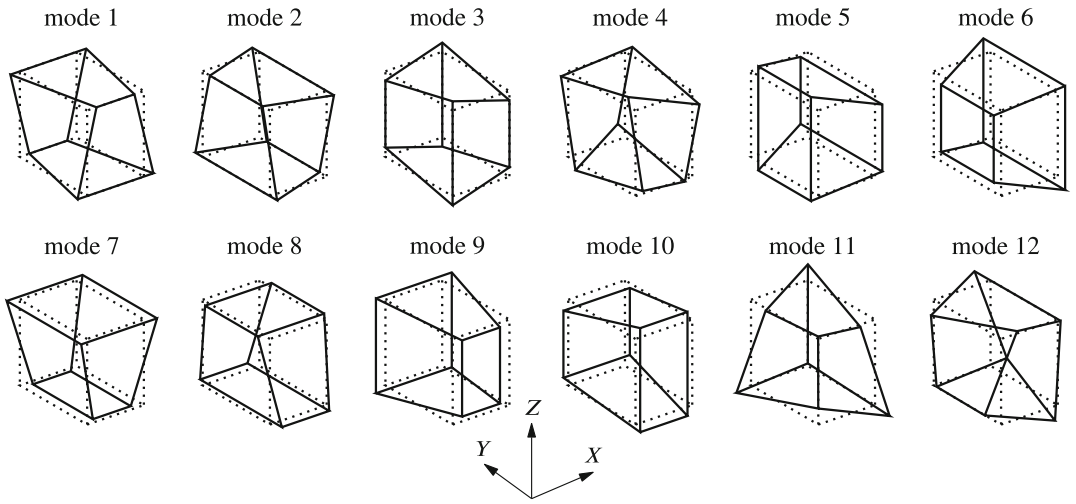

FIGURE 10 Eigenmodes in 3D with non-constant strain field (solid line) of H1U/h12 for the deformation state $\lambda_1 = 0.75$ (dotted). Computed using the Ogden material model.

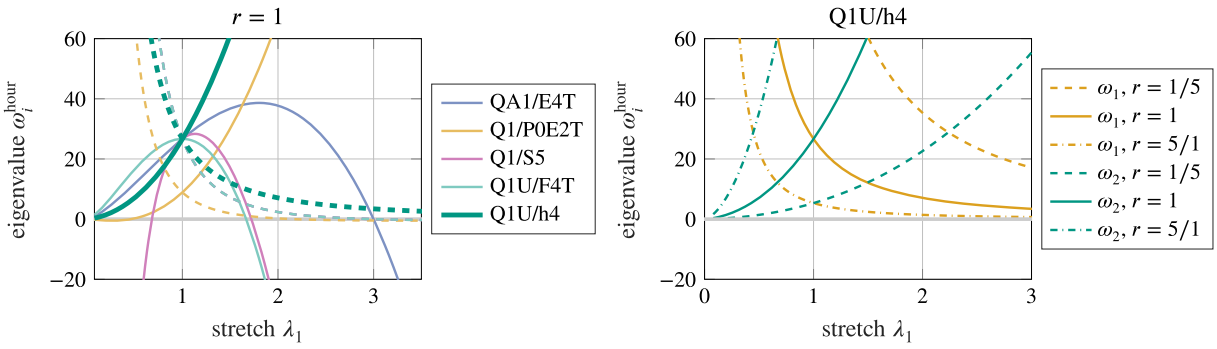

FIGURE 11 Results of the 2D one element stability analysis. Left: Eigenvalues ω_1^{hour} (dashed) and ω_2^{hour} (solid) for various elements with $r = 1$. Right: Eigenvalues ω_i^{hour} of Q1U/h4 for various r.

exhibit the well-known instability of ω_2^{hour} (solid line) under compression ($\lambda_1 < 1$ implies compression) first discovered for EAS elements by Wriggers and Reese[46] (see also Viebahn et al.[29] for assumed stress elements). All other elements exhibit no negative eigenvalues under compression and are therefore not prone to hourglassing.

In case of tension ($\lambda_1 > 1$) instabilities can be observed due to the material instability. In fact, the only EAS element without zero eigenvalue is the newly proposed Q1U/h4. Interestingly, the zeros of the other elements occur at $\lambda_1 \approx 1.75$ and $\lambda_1 \approx 3$ which coincides with instability points of the Ogden material. This supports the claim that the material instabilities transfer to the hourglass modes and cause the hourglassing patterns.[10] Hourglass mode ω_1^{hour} (dashed line) also becomes negative for some finite elements under tension but not for Q1U/h4.

The second plot of Figure 11 shows the hourglassing eigenvalues of Q1U/h4 with various element aspect ratios r. As mentioned above, some unsymmetric finite elements exhibit instabilities for rectangular elements even if they are stable for the quadratic element. This is, for example, the case if $\mathbf{F}^{\text{h},e}$ is used instead of $\mathbf{F}_0$ in (22). Fortunately, Q1U/h4 does not suffer from such defects.

Figure 12 shows results of the 3D one element stability test for the elements H1/P06T, H1U/F12, and H1U/h12. The eigenmodes 3, 9, and 10 are not included in the plots since they are duplicates[†††] of 2, 7, and 8, respectively. Almost all elements (not only the plotted) exhibit an instability for mode 12. The only exemption is the newly proposed H1U/h12 which is an interesting result even if mode 12 does usually not lead to global hourglassing patterns since it is incompatible to neighboring elements.[17] The most important modes 5–8, which are usually responsible for hourglassing, are highlighted with continuous lines in the plots. As expected, H1U/F12 exhibits instabilities both in compression (modes 5 and 6) and tension (mode 6). The instability of H1/P0E6T under compression in mode 6 does

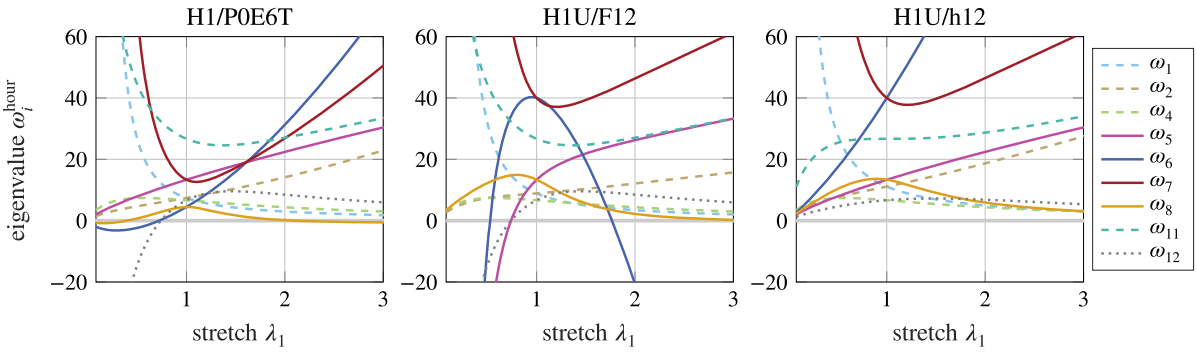

FIGURE 12 Results of the 3D one element stability analysis for $r = 1$. Hourglass eigenvalues for the Ogden material and H1/P0E6T (left), H1U/F12 (middle), and H1U/h12 (right).

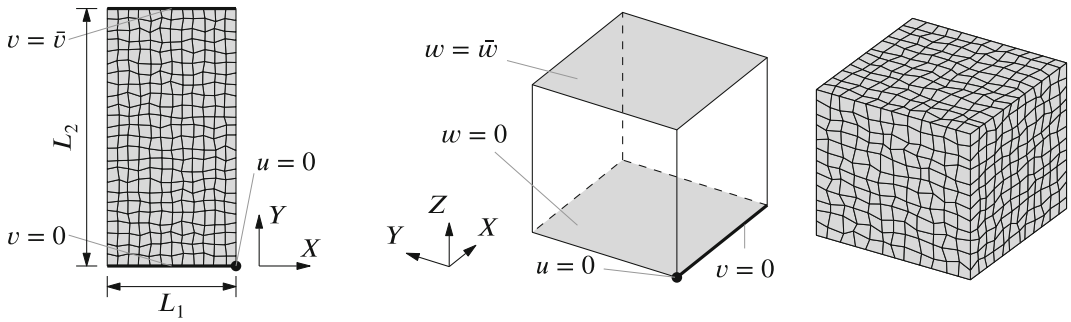

FIGURE 13 Setup and mesh of the large mesh stability analysis. Setup of 2D test with distorted mesh (left), setup for the 3D test (middle), and 3D distorted mesh (right).

not seem to play any role in hourglassing problems. However, mode 8, which becomes "slightly" instable under tension, likely explains the hourglassing of H1/P0E6T observed in the elasto-plastic simulation shown in Section 5.9. Furthermore, the too soft bending behavior of H1/P0E6T (see Section 5.2) is resembled by the comparably soft behavior (low eigenvalue) of mode 7. The 3D results described for H1/P0E6T and H1U/F12 are inline with the observation by Hille et al.[59] for the elasto-plastic material. Both elements show hourglassing in such simulations. In contrast to that, the novel element H1U/h12 does not suffer from any instabilities in this test. While this is not enough to immediately conclude that H1U/h12 is completely stable (there could e.g., be hourglassing in combination with neighboring elements), the simulations presented in the next sections further support the much improved stability of H1U/h12.

5.10 | Large mesh stability analysis

In addition to the one element stability analysis in Section 5.6, we present a test on larger FE-meshes in this section. We focus on a 2D problem which is discussed in depth in the work of Bieber et al.[62] and particularly interesting since there exists an *analytic* solution[71,95] of the considered diffuse bifurcation problem.

The 2D version of the test is performed on the rectangular[‡‡‡] block shown in Figure 13 with dimensions $L_1 = 25$ and $L_2 = 50$. The block is supported on the lower and top edge by the boundary conditions given in Figure 13 and is meshed with a regular or distorted mesh with 12×24 elements. The distortion is applied by randomly shifting all coordinates $|X_i - \overline{X}_i| \neq L_i/2$, where $\overline{X}_i$ is the block's center by $\Delta_i \in [-0.5, 0.5]$ such that the surface is maintained. In order to also cover instabilities under tension the Ogden material (66b) is considered with the parameters $\beta = 2, \kappa = 3.333 \cdot 10^3, n_p = 1$, $\alpha_1 = 0.5$ and $\mu_1 = 1.379 \cdot 10^3$ (corresponding to $E = 1000$ and $\nu = 0.45$) which are chosen such that a material instability arises (cf. Section 5.6).

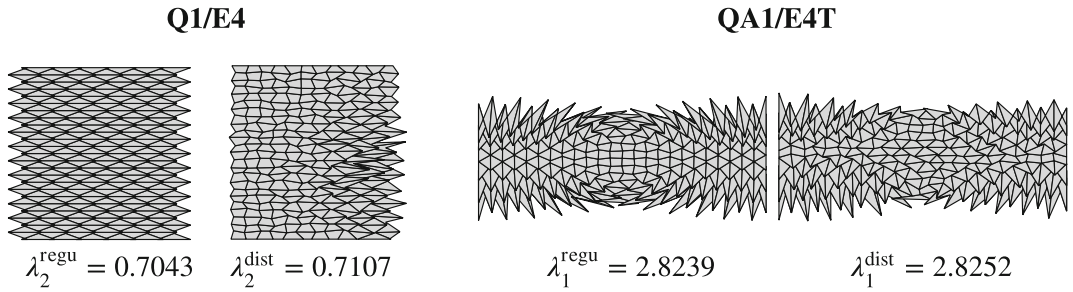

FIGURE 14 Results of the 2D large mesh stability analysis. Typical spurious modes for Q1/E4 under compression and QA1/E4T under tension (tension modes rotated by 90° and scaled in Y-direction by factor 4).

The actual stability analysis is performed by gradually de-/increasing the principal stretch in Y-direction by initially $\Delta\lambda = -0.01$ and $\Delta\lambda = +0.04$ in tension and compression, respectively. During that process the eigenvalues with lowest magnitude and the corresponding eigenvectors $\boldsymbol{\Phi}$ are computed numerically and tracked throughout the simulation which can be achieved by associating the current eigenvectors with the corresponding eigenvectors from the previous load step. The step width $\Delta\lambda$ is automatically adapted to ensure that the correct eigenmodes are associated with each other. Whenever an eigenvalue changes its sign we start an *extended system* solver.[69] The especially taylored version used here solves

$$\begin{bmatrix} \boldsymbol{\varphi}^{\text{h}} - \boldsymbol{\varphi}^{\text{ana}}(\lambda) \\ \mathbf{K}_{\text{red}}\boldsymbol{\Phi} + \alpha\boldsymbol{\Phi} \\ ||\boldsymbol{\Phi}||^2 - 1 \\ 0.5\alpha^2 \end{bmatrix} = \mathbf{0} \tag{74}$$

for the unknowns $\boldsymbol{\varphi}^{\text{h}}$, $\boldsymbol{\Phi}$, α, λ which accurately determines the instability point with zero-eigenvalue and corresponding eigenmode $\boldsymbol{\Phi}$ as well as the critical stretch λ. In the equation above $\mathbf{K}_{\text{red}}$ is the stiffness matrix where Dirichlet boundary conditions have been eliminated, $\boldsymbol{\varphi}^{\text{ana}}$ the analytic solution of the homogeneous problem (see Section 5.6) and α is a regularization parameter which iterates to zero and is used to avoid ill-conditioning of the tangential matrix of (74). To compute the derivative of the stiffness matrix $\mathbf{K}$ required for the Newton-scheme we employ the numerical tangent procedure proposed by Wriggers and Simo.[96] The entire process is repeated until four instabilities have been found.

Figure 14 shows the first two modes of Q1/E4 under compression and QA1/E4T under tension, respectively. These elements exhibit typical spurious (hourglassing) modes which occur similarly for all standard and PG-EAS elements which do not employ h-enhancement. In particular, Q1/E4, Q1/S5, Q1U/E4, and Q1U/F4 exhibit instabilities under compression and tension while QA1/E4T, Q1/P0E2T, and Q1U/F4T show no instabilities in the first four eigenmodes under compression but become unstable under tension due to the material instability. The only standard finite element, that works well in this test, is Q1/P0 which yields similar results as Q1U/h4 described below. These results are inline with Section 5.6.

The first two eigenmodes obtained with Q1U/h4 and corresponding analytically computed physical instabilities are shown in Figure 15. The analytic solution has first been proposed by Ogden[71] and is summarized well by Triantafyllidis et al.[95] We also refer to Bieber et al.[62] for in depth discussions and comparison of the analytical results to many standard finite element models. The numerical results of Q1U/h4 depicted in Figure 15 clearly show that Q1U/h4 performs extremely well in this test. It reproduces the analytic results in terms of both the mode shapes and level of stretch at which the eigenmodes occur with high accuracy. The same holds also for the third mode (not shown) with the exemption of the third compression mode in combination with the distorted mesh. Only the fourth mode shape differs from the analytic result. Most importantly, no spurious modes have been observed for Q1U/h4 in all four modes.

For the 3D version of this test we study a cube with edge length of 50 and the boundary conditions shown in Figure 13. Similar to the 2D case we employ both a regular mesh with $12 \times 12 \times 12$ elements and a distorted mesh obtained by randomly shifting the nodes by $\Delta_i \in [-1, 1]$ (the same amount as in the 2D case in relation to the element size). The

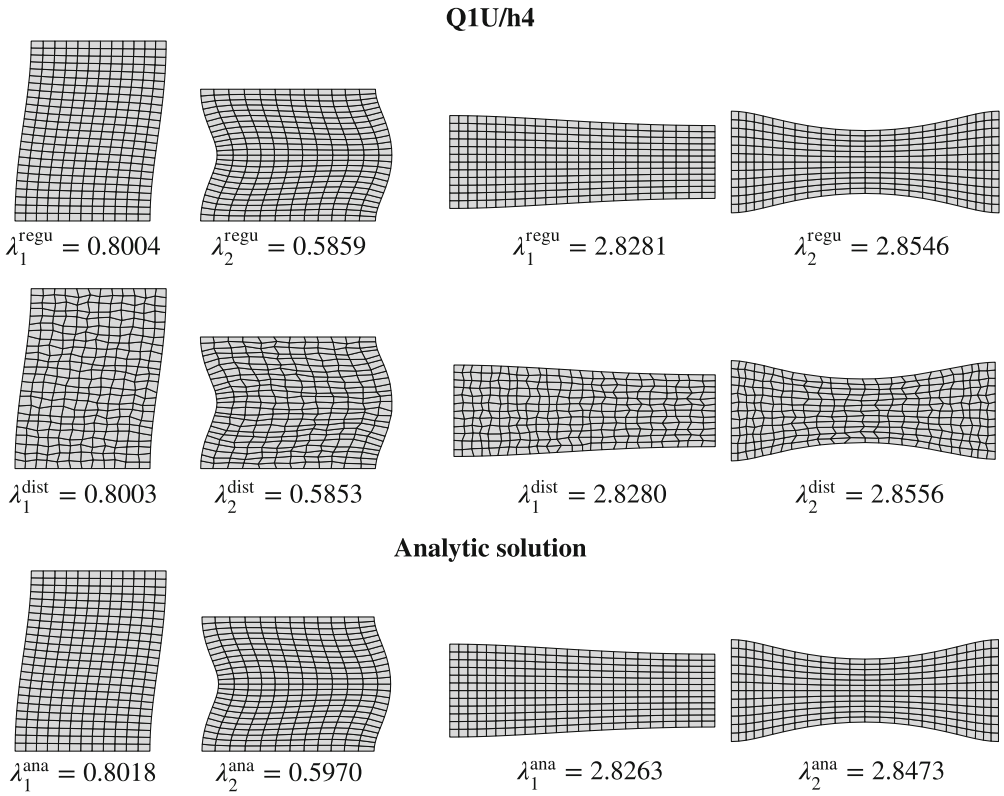

FIGURE 15 First two eigenmodes and corresponding critical stretches $\lambda_i^{(\bullet)}$ for the 2D large mesh stability analysis computed with Q1U/h4 for a regular (λ_i^{regu}, top row) and distorted mesh (λ_i^{dist}, middle row) are compared to the analytic solution (λ_i^{ana}, bottom row). All modes in tension are rotated by 90° and scaled in the Y-direction by factor 4.

resulting eigenmodes computed with H1U/h12 are shown in Figure 16. Again, there are no spurious modes similar to the 2D case. Furthermore, the mode shapes as well as the critical stretches differ only slightly for the two meshes which highlights once more the mesh distortion insensitivity of the Petrov–Galerkin approach.

5.11 | Necking of a plane strain elasto-plastic plate

The final two examples in this work are elasto-plastic necking simulations which are well-known[59] to trigger hourglassing for standard elements. First we consider a plate subjected to plane strain conditions[2,10,14,47,54,89] with length $2L = 53.334$, width $2R = 12.826$ and thickness $t = 1$. Only one fourth (see Figure 17) has to be modeled due to symmetry and is meshed with $20 \times 10 \times 1$ elements. Boundary conditions $u(X = 0, X, Z) = 0$, $v(X, Y = 0, Z) = 0$ and $w(X, Y, Z) = 0$ ensure symmetry and the plane strain state, respectively. Load is applied at the top edge in the form of prescribed displacements $\bar{u} = 7$ applied within 200 load steps[§§§]. Furthermore, a geometric imperfection in the form of a linear reduction of the width to $\overline{R} = 6.343$ ensures that necking initiates at the lower boundary ($Y = 0$). Figure 17 shows the initial geometry, boundary conditions, mesh with refinement in the lower fifth and a typical load displacement curve.

Results of the test are shown in Figure 18 which depicts a deformed configuration computed with different finite elements at $\bar{u} = 5.6$. It is clearly visible that H1/E9 shows severe hourglassing. HA1/E12T's spurious mode is less pronounced due to the special nine point integration yet it can still be seen especially along the left edge. If the standard Gauss quadrature was employed the hourglassing patterns would be similar to H1/E9. PG-EAS elements based on F- and E-enhancement do not converge in this test and show severe hourglassing before the Newton–Raphson scheme fails. Only the mixed pressure EAS element H1/P0E6T and the newly proposed h-enhanced H1U/h12 are hourglassing-free. Especially the latter result is very interesting. To the best knowledge of the authors this is the first EAS element to be hourglassing-free in this test.

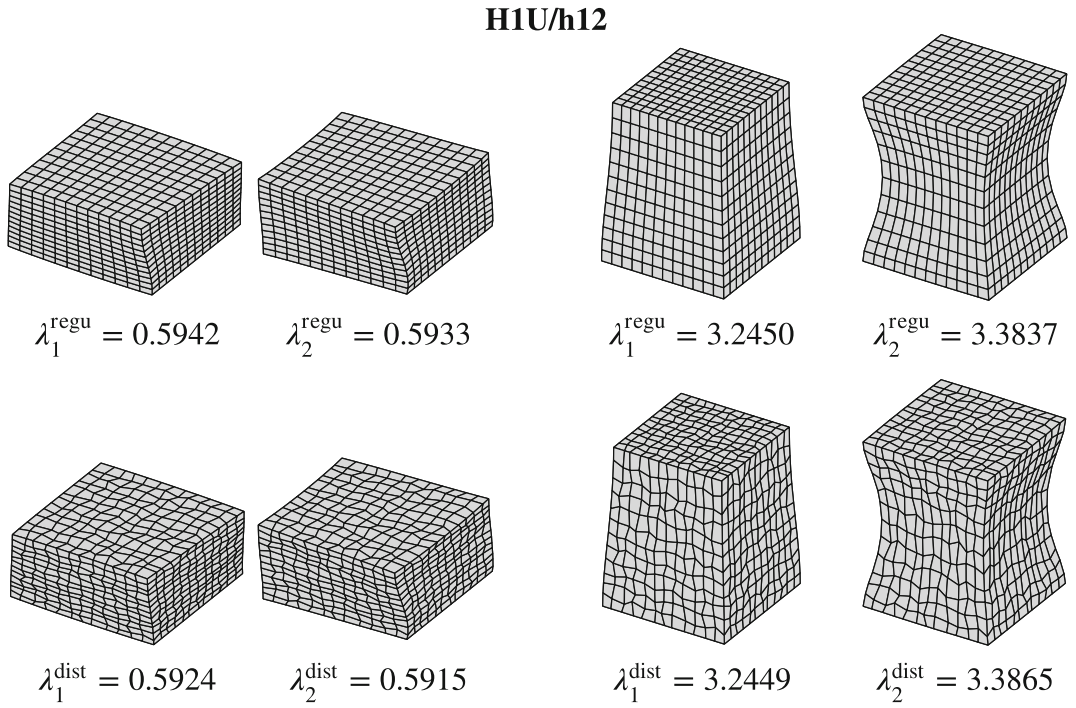

FIGURE 16 First two eigenmodes and corresponding critical stretches $\lambda_i^{(\bullet)}$ for the 3D large mesh stability analysis computed with H1U/h12 for a regular (λ_i^{regu}, top row) and distorted mesh (λ_i^{dist}, bottom row). Modes in tension are scaled in the Z-direction by factor 4.

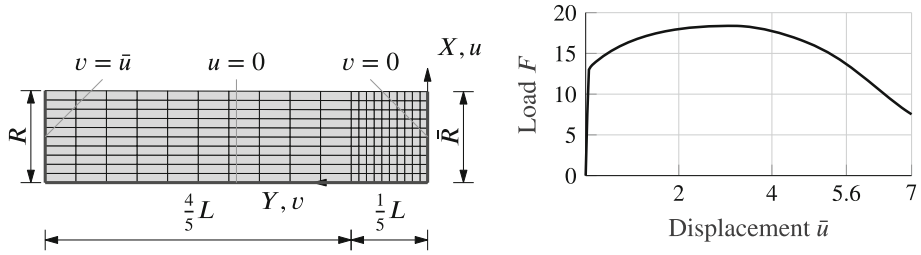

FIGURE 17 Setup of the plane strain elasto-plastic plate example (left) and load displacement curve computed with H1U/h12 (right).

5.12 | Necking of a elasto-plastic circular bar

The final benchmark in this work concerns the necking of an elasto-plastic circular bar.[2,5,14,17,19,88] Similar to the previous simulation we consider a cylindric specimen with length $2L = 53.334$ and radius $R = 6.413$ of which only one eight is considered due to symmetry. Figure 19 shows the undeformed geometry and the mesh which consists of two parts with 480 elements each. Symmetry boundary conditions $u = 0$, $v = 0$, $w = 0$ apply on the surfaces $X = 0$, $Y = 0$, $Z = 0$, respectively, and load is applied by prescribed displacement $u = \bar{u}$ on the surface $X = L$. Again, the radius is linearly reduced to $\overline{R} = 6.343$ to initiate necking at $X = 0$. The final state $\bar{u} = 7$ is reached within 30 load steps[¶¶¶] of which half is used up to a displacement of $\bar{u} = 5.6$ and the other half is used to cover the more demanding range up to $\bar{u} = 7.0$.

Figure 19 shows the load displacement curves for several finite elements. Element H1/P0 is taken as reference solution since it coincides well with experimental data.[97] Apart from H1/P0E6T the curves are pretty much the same up to $\bar{u} \approx 5.6$ with a maximum load of $F_{\max} = 77.65 \pm 0.1\%$. Afterwards, there are slight differences with H1U/h12 exhibiting the best agreement with H1/P0. Figure 20 shows the final configuration for $\bar{u} = 7.0$ computed with various elements. Only H1/P0E6T exhibits spurious hourglassing modes. Thus, to the best knowledge of the authors, H1U/h12 is the only low-order locking-free finite element to be hourglassing-free in both the plane strain (see Section 5.8) and circular bar elasto-plastic necking simulation.

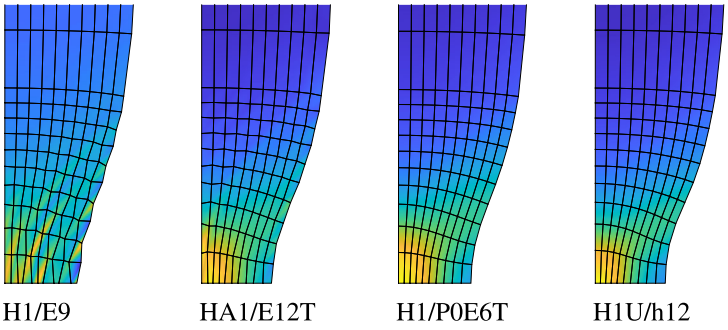

FIGURE 18 Results of the plane strain elasto-plastic plate test. Deformed configuration with distribution of accumulated plastic strain for prescribed displacement $\bar{u} = 5.6$.

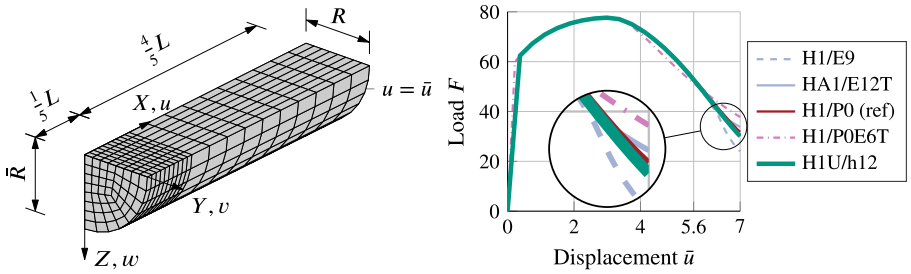

FIGURE 19 Setup of the elasto-plastic circular bar example (left) and load displacement curve for various elements (right).

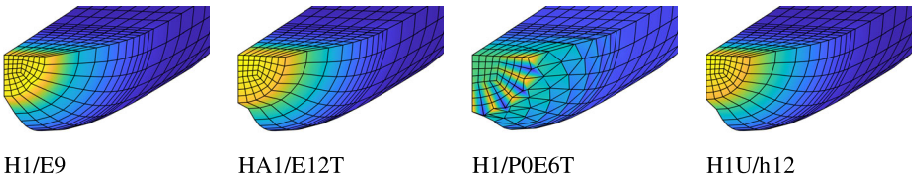

FIGURE 20 Results of circular bar necking test. Deformed configuration with distribution of accumulated plastic strain for prescribed displacement $\bar{u} = 7.0$.

6 | CONCLUSION

The present contribution introduced a novel *Petrov–Galerkin EAS element* for large deformation solid mechanics. It is based on the recently published linear elastic framework by the authors[18] and *enhancement of the spatial displacement gradient*.[64] The resulting element has many favorable properties. Besides the standard requirements such as satisfaction of the patch test, objectivity and being locking-free it exhibits two outstanding features. First, the Petrov–Galerkin approach makes the finite element much less sensitive to mesh distortion. This is of great value in practical simulations since it could reduce the effort needed to mesh complex geometries. Second, the finite element is free from spurious modes in all typically critical examples known to trigger hourglassing for existing finite elements. In fact it is to the best knowledge of the authors the *only* locking-free low-order mixed finite element to be free from hourglassing under compression, tension and for elasto-plastic simulations. Moreover, we postulated a hypothesis on why instabilities arise for all previously proposed EAS elements and other related mixed methods. We supposed that the transmission of well-known checkerboard modes to the enhanced modes is at the core of the problem and showed that the newly proposed approach circumvents the issue.

Two further novelties in the present work concern a slight modification of the higher order enhanced modes and the MIP-method first used for Petrov–Galerkin elements in this contribution. The former reduced the numerical effort to get the ansatz functions and the latter increased robustness of the approach in the Newton–Raphson scheme. Finally,

we tested the novel element in a plethora of examples and showed that it outperforms the standard elements used for comparison.

Future work could first focus on tackling the spurious behavior in the mesh distortion test for non-standard meshes mentioned in Remark 6. Furthermore, despite the progress made with the MIP method, it would be interesting to further increase the element's robustness to achieve the same performance as assumed stress elements in that regard. Naturally, it would also be valuable to find a proof for the hypothesis on stability of the element. However, we believe that it would be of the utmost interest to apply the methods developed herein to shell elements.

ACKNOWLEDGMENTS

We thank Simon Bieber (University of Stuttgart) for his valuable input and for sharing his research on the numeric and analytic large mesh stability analysis. This work was funded by the Deutsche Forschungsgemeinschaft (DFG, German Research Foundation) – project number 466086399. This support is gratefully acknowledged. Open Access funding enabled and organized by Projekt DEAL.

DATA AVAILABILITY STATEMENT

The data that support the findings of this study are available from the corresponding author upon reasonable request.

ENDNOTES

*Here and subsequently we frequently omit arguments of functions in favor of a more concise notation.

†The same holds for example, also for the EAS element by Glaser and Armero[10] due to the transformation needed for objectivity.

‡Here and subsequently we use superscript $(\bullet)^{\mathrm{h}}$ to denote finite element discretizations.

§Shape functions constructed in the physical space are in general termed metric shape functions.[37]

¶Invariance to node numbering, see Section 4.2.

‖For various types of nonlinear mixed elements which meet this requirement see, for example, References 2,5,10,29,78-80.

**It is not necessarily the only solution due to possible instabilities but it suffices to show that $\boldsymbol{\varphi}^{\mathrm{h},e} = \boldsymbol{\varphi}_{\mathrm{ho}}$ is *a* solution to prove that the patch test is fulfilled.

††See also Simo and Rifai's[1] design imperative for EAS elements on non-overlapping ansatz spaces of the actual displacement and the enhanced field.

‡‡For regular meshes with constant Jacobian $\mathbf{J}^{\mathrm{h},e} = \mathbf{J}_0$ the fields are automatically orthogonal. Otherwise, the correction for no nodal contribution of the enhanced modes in (33) and the bilinear modes in (34) induce a non-orthogonality.

§§The volumetric-deviatoric split of a Cauchy stress tensor $\boldsymbol{\sigma} = dev(\boldsymbol{\sigma}) - p^{\mathrm{h},e}\mathbf{I}$ and the transformation $\boldsymbol{\tau} = \det(\mathbf{F})\boldsymbol{\sigma}$ imply that $p_0^{\mathrm{h},e}$ is directly related to piecewise constant "physical" pressure $p^{\mathrm{h},e}$. This holds because $\det(\mathbf{F})$ is also piecewise constant due to the fact that the pressure is usually a function of $\det(\mathbf{F})$ alone.

¶¶Element names in parentheses denote corresponding 2D elements.

‖‖See also Sussmann and Bathe[15] who show that instabilities can even occur for small deformations if the element's aspect ratio is high.

***If the matrix is truly diagonal can be used to check if the test is performed correctly and verify that $\mathbb{P}^{\mathrm{hour}}$ are actually eigenvectors of $\mathbf{K}^e$.

†††Figure 10 indicates this since the corresponding modes are merely a rotation of each other around the x-axis.

‡‡‡The rectangular shape makes it easier to compute the exact instability points since the (physical) modes do not all appear at almost the same load level.[62]

§§§This large number of load steps is necessary to capture the hourglass behavior. Elements that do not exhibit spurious modes converge much faster. In particular, the novel H1U/h12 requires 28 load steps.

¶¶¶Only element H1/P0E6T requires a total of 50 load steps due to the hourglassing patterns.

ORCID

Robin Pfefferkorn https://orcid.org/0000-0002-2153-1236
Peter Betsch https://orcid.org/0000-0002-0596-2503

REFERENCES

1. Simo JC, Rifai MS. A class of mixed assumed strain methods and the method of incompatible modes. *Int J Numer Methods Eng*. 1990;29(8):1595-1638. doi:10.1002/nme.1620290802
2. Simo JC, Armero F. Geometrically non-linear enhanced strain mixed methods and the method of incompatible modes. *Int J Numer Methods Eng*. 1992;33(7):1413-1449. doi:10.1002/nme.1620330705
3. Wilson EL, Taylor RL, Doherty WP, Ghaboussi J. Incompatible displacement models. In: Fenves SJ, Perrone N, Robinson AR, eds. *Numerical and Computer Methods in Structural MechanicsNew*. Elsevier; 1973:43-57.
4. Taylor RL, Beresford PJ, Wilson EL. A non-conforming element for stress analysis. *Int J Numer Methods Eng*. 1976;10(6):1211-1219. doi:10.1002/nme.1620100602

5. Simo JC, Armero F, Taylor RL. Improved versions of assumed enhanced strain tri-linear elements for 3D finite deformation problems. *Comput Methods Appl Mech Eng*. 1993;110(3-4):359-386. doi:10.1016/0045-7825(93)90215-J
6. Crisfield MA, Moita GF, Jelenić G, Lyons LPR. Enhanced lower-order element formulations for large strains. *Comput Mech*. 1995;17(1):62-73. doi:10.1007/BF00356479
7. Korelc J, Wriggers P. Consistent gradient formulation for a stable enhanced strain method for large deformations. *Eng Comput*. 1996;13(1):103-123. doi:10.1108/02644409610111001
8. Korelc J, Wriggers P. An efficient 3D enhanced strain element with Taylor expansion of the shape functions. *Comput Mech*. 1996;19(2):30-40. doi:10.1007/BF02757781
9. Wriggers P, Korelc J. On enhanced strain methods for small and finite deformations of solids. *Comput Mech*. 1996;18(6):413-428. doi:10.1007/BF00350250
10. Glaser S, Armero F. On the formulation of enhanced strain finite elements in finite deformations. *Eng Comput*. 1997;14(7):759-791. doi:10.1108/02644409710188664
11. Klinkel S, Wagner W. A geometrical non-linear brick element based on the EAS-method. *Int J Numer Methods Eng*. 1997;40(24):4529-4545. doi:10.1002/(SICI)1097-0207(19971230)40:24<4529::AID-NME271>3.0.CO;2-I
12. Korelc J, Wriggers P. Improved enhanced strain four-node element with Taylor expansion of the shape functions. *Int J Numer Methods Eng*. 1997;40(3):407-421. doi:10.1002/(SICI)1097-0207(19970215)40:3<407::AID-NME70>3.0.CO;2-P
13. Müller-Hoeppe DS, Löhnert S, Wriggers P. A finite deformation brick element with inhomogeneous mode enhancement. *Int J Numer Methods Eng*. 2009;78(10):1164-1187. doi:10.1002/nme.2523
14. Korelc J, Šolinc U, Wriggers P. An improved EAS brick element for finite deformation. *Comput Mech*. 2010;46(4):641-659. doi:10.1007/s00466-010-0506-0
15. Sussman T, Bathe KJ. Spurious modes in geometrically nonlinear small displacement finite elements with incompatible modes. *Comput Struct*. 2014;140:14-22. doi:10.1016/j.compstruc.2014.04.004
16. Pfefferkorn R, Betsch P. On transformations and shape functions for enhanced assumed strain elements. *Int J Numer Methods Eng*. 2019;120(2):231-261. doi:10.1002/nme.6133
17. Pfefferkorn R, Betsch P. Extension of the enhanced assumed strain method based on the structure of polyconvex strain-energy functions. *Int J Numer Methods Eng*. 2020;121(8):1695-1737. doi:10.1002/nme.6284
18. Pfefferkorn R, Betsch P. Mesh distortion insensitive and locking-free Petrov-Galerkin low-order EAS elements for linear elasticity. *Int J Numer Methods Eng*. 2021;122(23):6924-6954. doi:10.1002/nme.6817
19. Pfefferkorn R, Bieber S, Oesterle B, Bischoff M, Betsch P. Improving efficiency and robustness of EAS elements for nonlinear problems. *Int J Numer Methods Eng*. 2021;122(8):1911-1939. doi:10.1002/nme.6605
20. Büchter N, Ramm E, Roehl D. Three-dimensional extension of non-linear shell formulation based on the enhanced assumed strain concept. *Int J Numer Methods Eng*. 1994;37(15):2551-2568. doi:10.1002/nme.1620371504
21. Betsch P, Gruttmann F, Stein E. A 4-node finite shell element for the implementation of general hyperelastic 3D-elasticity at finite strains. *Comput Methods Appl Mech Eng*. 1996;130(1):57-79. doi:10.1016/0045-7825(95)00920-5
22. Andelfinger U, Ramm E. EAS-elements for two-dimensional, three-dimensional, plate and shell structures and their equivalence to HR-elements. *Int J Numer Methods Eng*. 1993;36(8):1311-1337. doi:10.1002/nme.1620360805
23. Armero F, Linder C. New finite elements with embedded strong discontinuities in the finite deformation range. *Comput Methods Appl Mech Eng*. 2008;197(33-40):3138-3170. doi:10.1016/j.cma.2008.02.021
24. Linder C, Armero F. Finite elements with embedded strong discontinuities for the modeling of failure in solids. *Int J Numer Methods Eng*. 2007;72(12):1391-1433. doi:10.1002/nme.2042
25. Krischok A, Linder C. On the enhancement of low-order mixed finite element methods for the large deformation analysis of diffusion in solids. *Int J Numer Methods Eng*. 2016;106(4):278-297. doi:10.1002/nme.5120
26. Pfefferkorn R, Betsch P. Open issues on the EAS method and mesh distortion insensitive locking-free low-order unsymmetric EAS elements. Proceedings of the 14th WCCM-ECCOMAS Congress 2020; 2021; Paris, France. doi:10.23967/wccm-eccomas.2020.264
27. Garcea G, Trunfio GA, Casciaro R. Mixed formulation and locking in path-following nonlinear analysis. *Comput Methods Appl Mech Eng*. 1998;165(1):247-272. doi:10.1016/S0045-7825(98)00068-1
28. Magisano D, Leonetti L, Garcea G. Advantages of the mixed format in geometrically nonlinear analysis of beams and shells using solid finite elements. *Int J Numer Methods Eng*. 2016;109(9):1237-1262. doi:10.1002/nme.5322
29. Viebahn N, Schröder J, Wriggers P. An extension of assumed stress finite elements to a general hyperelastic framework. *Adv Model Simul Eng Sci*. 2019;6(9):1-9. doi:10.1186/s40323-019-0133-z
30. Magisano D, Leonetti L, Garcea G. How to improve efficiency and robustness of the Newton method in geometrically non-linear structural problem discretized via displacement-based finite elements. *Comput Methods Appl Mech Eng*. 2017;313:986-1005. doi:10.1016/j.cma.2016.10.023
31. MacNeal RH. On the limits of finite element perfectability. *Int J Numer Methods Eng*. 1992;35(8):1589-1601. doi:10.1002/nme.1620350804
32. MacNeal RH. A theorem regarding the locking of tapered four-noded membrane elements. *Int J Numer Methods Eng*. 1987;24(9):1793-1799. doi:10.1002/nme.1620240913
33. Rajendran S, Liew KM. A novel unsymmetric 8-node plane element immune to mesh distortion under a quadratic displacement field. *Int J Numer Methods Eng*. 2003;58(11):1713-1748. doi:10.1002/nme.836
34. Rajendran S. A technique to develop mesh-distortion immune finite elements. *Comput Methods Appl Mech Eng*. 2010;199(17):1044-1063. doi:10.1016/j.cma.2009.11.017

35. Ooi ET, Rajendran S, Yeo JH. Remedies to rotational frame dependence and interpolation failure of US-QUAD8 element. *Commun Numer Methods Eng*. 2008;24(11):1203-1217. doi:10.1002/cnm.1026
36. Xie Q, Sze KY, Zhou YX. Modified and Trefftz unsymmetric finite element models. *Int J Mech Mater Des*. 2016;12(1):53-70. doi:10.1007/s10999-014-9289-3
37. MacNeal RH. *Finite Elements: Their Design and Performance*. Dekker; 1994.
38. Cen S, Zhou PL, Li CF, Wu CJ. An unsymmetric 4-node, 8-dof plane membrane element perfectly breaking through MacNeal's theorem. *Int J Numer Methods Eng*. 2015;103(7):469-500. doi:10.1002/nme.4899
39. Zhou PL, Cen S, Huang JB, Li CF, Zhang Q. An unsymmetric 8-node hexahedral element with high distortion tolerance. *Int J Numer Methods Eng*. 2017;109(8):1130-1158. doi:10.1002/nme.5318
40. Li Z, Cen S, Wu CJ, Shang Y, Li CF. High-performance geometric nonlinear analysis with the unsymmetric 4-node, 8-DOF plane element US-ATFQ4. *Int J Numer Methods Eng*. 2018;114(9):931-954. doi:10.1002/nme.5771
41. Li Z, Cen S, Huang J, Li CF. Hyperelastic finite deformation analysis with the unsymmetric finite element method containing homogeneous solutions of linear elasticity. *Int J Numer Methods Eng*. 2020;121:3702-3721. doi:10.1002/nme.6378
42. Li Z, Cen S, Li C. Extension of the unsymmetric 8-node hexahedral solid element US-ATFH8 to geometrically nonlinear analysis. *Eng Comput*. 2021;38(8):3219-3253. doi:10.1108/EC-04-2020-0203
43. Huang Y, Huan Y, Chen H. An incompatible and unsymmetric four-node quadrilateral plane element with high numerical performance. *Int J Numer Methods Eng*. 2020;121(15):3382-3396. doi:10.1002/nme.6363
44. Huang YQ, Yang YF, Wang JZ, Liu XC, Chen HB. Unsymmetric extensions of Wilson's incompatible four-node quadrilateral and eight-node hexahedral elements. *Int J Numer Methods Eng*. 2021;123(1):101-127. doi:10.1002/nme.6849
45. Nadler B, Rubin MB. A new 3-D finite element for nonlinear elasticity using the theory of a cosserat point. *Int J Solids Struct*. 2003;40(17):4585-4614. doi:10.1016/S0020-7683(03)00210-5
46. Wriggers P, Reese S. A note on enhanced strain methods for large deformations. *Comput Methods Appl Mech Eng*. 1996;135(3-4):201-209. doi:10.1016/0045-7825(96)01037-7
47. de Souza Neto EA, Perić D, Huang GC, Owen DRJ. Remarks on the stability of enhanced strain elements in finite elasticity and elastoplasticity. *Commun Numer Methods Eng*. 1995;11(11):951-961. doi:10.1002/cnm.1640111109
48. Glaser S, Armero F. *Recent developments in the formulation of assumed enhanced strain finite elements for finite deformation problems*. UCB/SEMM Report 95/13, University of California; Berkeley, CA: 1995.
49. Areias PM, César de Sá JM, António CC, Fernandes AA. Analysis of 3D problems using a new enhanced strain hexahedral element. *Int J Numer Methods Eng*. 2003;58(11):1637-1682. doi:10.1002/nme.835
50. Reese S, Wriggers P. A stabilization technique to avoid hourglassing in finite elasticity. *Int J Numer Methods Eng*. 2000;48(1):79-109. doi:10.1002/(SICI)1097-0207(20000510)48:1<79::AID-NME869>3.0.CO;2-D
51. Wall WA, Bischoff M, Ramm E. A deformation dependent stabilization technique, exemplified by EAS elements at large strains. *Comput Methods Appl Mech Eng*. 2000;188(4):859-871. doi:10.1016/S0045-7825(99)00365-5
52. Reese S. On a physically stabilized one point finite element formulation for three-dimensional finite elasto-plasticity. *Comput Methods Appl Mech Eng*. 2005;194(45):4685-4715. doi:10.1016/j.cma.2004.12.012
53. Armero F. A modal analysis of finite deformation enhanced strain finite elements. UCB/SEMM Report 96/03, University of California; Berkeley, CA; 1996.
54. Armero F. On the locking and stability of finite elements in finite deformation plane strain problems. *Comput Struct*. 2000;75(3):261-290. doi:10.1016/s0045-7949(99)00136-4
55. Caylak I, Mahnken R. Stabilization of mixed tetrahedral elements at large deformations. *Int J Numer Methods Eng*. 2012;90(2):218-242. doi:10.1002/nme.3320
56. Pantuso D, Bathe KJ. On the stability of mixed finite elements in large strain analysis of incompressible solids. *Finite Elem Anal Des*. 1997;28(2):83-104. doi:10.1016/S0168-874X(97)81953-1
57. Kasper EP, Taylor RL. A mixed-enhanced strain method. Part I: geometrically linear problems. *Comput Struct*. 2000;75(3):237-250. doi:10.1016/S0045-7949(99)00134-0
58. Kasper EP, Taylor RL. A mixed-enhanced strain method. Part II: geometrically nonlinear problems. *Comput Struct*. 2000;75(3):251-260. doi:10.1016/S0045-7949(99)00135-2
59. Hille M, Pfefferkorn R, Betsch P. Locking-free mixed finite element methods and their spurious hourglassing patterns. In: Aldakheel F, Hudobivnik B, Soleimani M, Wessels H, Weißenfels C, Marino M, eds. *Current Trends and Open Problems in Computational Mechanics*. Springer; 2022:181-194.
60. Moita GF. *Non-Linear Finite Element Analysis of Continua with Emphasis on Hyperelasticity*. PhD thesis. Imperial College, London; 1994.
61. Fontes Valente RA, Alves de Sousa RJ, Natal Jorge RM. An enhanced strain 3D element for large deformation elastoplastic thin-shell applications. *Comput Mech*. 2004;34(1):38-52. doi:10.1007/s00466-004-0551-7
62. Bieber S, Auricchio F, Reali A, Bischoff M. Artificial instabilities of finite elements for finite elasticity: analysis and remedies. *Eng Arch (engrxiv)*. 2022:1-41. doi:10.31224/2604
63. Crisfield MA, Moita GF. A co-rotational formulation for 2-D continua including incompatible modes. *Int J Numer Methods Eng*. 1996;39(15):2619-2633. doi:10.1002/(SICI)1097-0207(19960815)39:15<2619::AID-NME969>3.0.CO;2-N
64. Schmied C. *Hocheffiziente und robuste finite Elemente niederer Ansatzordnung zur Simulation großer Deformationen von Festkörpern*. PhD thesis. Karlsruhe Institute of Technology (KIT), Karlsruhe; 2017.

65. Nagtegaal JC, Fox DD. Using assumed enhanced strain elements for large compressive deformation. *Int J Solids Struct*. 1996;33(20):3151-3159. doi:10.1016/0020-7683(95)00250-2
66. Klinkel S, Gruttmann F, Wagner W. A robust non-linear solid shell element based on a mixed variational formulation. *Comput Methods Appl Mech Eng*. 2006;195(1):179-201. doi:10.1016/j.cma.2005.01.013
67. Yuan KY, Huang YS, Pian THH. New strategy for assumed stresses for 4-node hybrid stress membrane element. *Int J Numer Methods Eng*. 1993;36(10):1747-1763. doi:10.1002/nme.1620361009
68. Wisniewski K, Turska E. Improved four-node Hellinger-Reissner elements based on skew coordinates. *Int J Numer Methods Eng*. 2008;76(6):798-836. doi:10.1002/nme.2343
69. Wriggers P. *Nonlinear Finite Element Methods*. Springer; 2008.
70. Belytschko T, Ong JSJ, Liu WK, Kennedy JM. Hourglass control in linear and nonlinear problems. *Comput Methods Appl Mech Eng*. 1984;43(3):251-276. doi:10.1016/0045-7825(84)90067-7
71. Ogden RW. *Non-Linear Elastic Deformations*. Dover Publ; 1997.
72. Haupt P. *Continuum Mechanics and Theory of Materials*. 2nd ed. Springer; 2002.
73. Holzapfel GA. *Nonlinear Solid Mechanics: A Continuum Approach for Engineering*. Wiley; 2000.
74. Pian THH, Sumihara K. Rational approach for assumed stress finite elements. *Int J Numer Methods Eng*. 1984;20(9):1685-1695. doi:10.1002/nme.1620200911
75. Sze KY, Chow CL, Wanji C. On invariance of isoparametric hybrid/mixed elements. *Commun Numer Methods Eng*. 1992;8(6):385-406. doi:10.1002/cnm.1630080605
76. Jabareen M, Rubin MB. A 3-D brick cosserat point element (CPE) for nonlinear elasticity. In: Silberschmidt VV, ed. *Computational and Experimental Mechanics of Advanced Materials*. Springer; 2010:83-140.
77. Hartmann S, Neff P. Polyconvexity of generalized polynomial-type hyperelastic strain energy functions for near-incompressibility. *Int J Solids Struct*. 2003;40(11):2767-2791. doi:10.1016/S0020-7683(03)00086-6
78. Angoshtari A, Faghih Shojaei M, Yavari A. Compatible-strain mixed finite element methods for 2D compressible nonlinear elasticity. *Comput Methods Appl Mech Eng*. 2017;313:596-631. doi:10.1016/j.cma.2016.09.047
79. Wisniewski K, Wagner W, Turska E, Gruttmann F. Four-node Hu-Washizu elements based on skew coordinates and contravariant assumed strain. *Comput Struct*. 2010;88(21):1278-1284. doi:10.1016/j.compstruc.2010.07.008
80. Simo JC, Taylor RL, Pister KS. Variational and projection methods for the volume constraint in finite deformation elasto-plasticity. *Comput Methods Appl Mech Eng*. 1985;51(1):177-208. doi:10.1016/0045-7825(85)90033-7
81. Zienkiewicz OC, Taylor RL, Zhu J. *The Finite Element Method. Vol. 1: Its Basis and Fundamentals*. 6th ed. Elsevier Butterworth-Heinemann; 2010.
82. Reddy BD, Simo JC. Stability and convergence of a class of enhanced strain methods. *SIAM J Numer Anal*. 1995;32(6):1705-1728. doi:10.1137/0732077
83. Boffi D, Brezzi F, Fortin M. *Mixed Finite Element Methods and Applications. Springer Series in Computational Mathematics*. Vol 44. Springer; 2013.
84. Lamichhane BP, Reddy BD, Wohlmuth BI. Convergence in the incompressible limit of finite element approximations based on the Hu-Washizu formulation. *Numer Math*. 2006;104(2):151-175. doi:10.1007/s00211-006-0014-5
85. Djoko JK, Lamichhane BP, Reddy BD, Wohlmuth BI. Conditions for equivalence between the Hu-Washizu and related formulations, and computational behavior in the incompressible limit. *Comput Methods Appl Mech Eng*. 2006;195(33):4161-4178. doi:10.1016/j.cma.2005.07.018
86. Pian THH, Tong P. Relations between incompatible displacement model and hybrid stress model. *Int J Numer Methods Eng*. 1986;22(1):173-181. doi:10.1002/nme.1620220112
87. Bonet J, Wood RD. *Nonlinear Continuum Mechanics for Finite Element Analysis*. 2nd ed. Cambridge University Press; 2008.
88. Simo JC. Algorithms for static and dynamic multiplicative plasticity that preserve the classical return mapping schemes of the infinitesimal theory. *Comput Methods Appl Mech Eng*. 1992;99(1):61-112.
89. Simo JC. A framework for finite strain elastoplasticity based on maximum plastic dissipation and the multiplicative decomposition. Part II: computational aspects. *Comput Methods Appl Mech Eng*. 1988;68(1):1-31. doi:10.1016/0045-7825(88)90104-1
90. Puso MA. A highly efficient enhanced assumed strain physically stabilized hexahedral element. *Int J Numer Methods Eng*. 2000;49(8):1029-1064. doi:10.1002/1097-0207(20001120)49:8<1029::AID-NME990>3.0.CO;2-3
91. Piltner R, Taylor RL. A quadrilateral mixed finite element with two enhanced strain modes. *Int J Numer Methods Eng*. 1995;38(11):1783-1808. doi:10.1002/nme.1620381102
92. Müller A, Bischoff M. A consistent finite element formulation of the geometrically non-linear Reissner-Mindlin shell model. *Arch Comput Meth Eng*. 2022;29(5):3387-3434. doi:10.1007/s11831-021-09702-7
93. Başar Y, Ding Y. Finite-rotation shell elements for the analysis of finite-rotation shell problems. *Int J Numer Methods Eng*. 1992;34(1):165-169. doi:10.1002/nme.1620340109
94. Liesen J, Mehrmann V. *Lineare Algebra*. Springer Spektrum; 2015.
95. Triantafyllidis N, Scherzinger WM, Huang HJ. Post-bifurcation equilibria in the plane-strain test of a hyperelastic rectangular block. *Int J Solids Struct*. 2007;44(11):3700-3719. doi:10.1016/j.ijsolstr.2006.10.012
96. Wriggers P, Simo JC. A general procedure for the direct computation of turning and bifurcation points. *Int J Numer Methods Eng*. 1990;30(1):155-176. doi:10.1002/nme.1620300110

97. Simo JC, Hughes TJR. *Computational Inelasticity. Volume 7 of Interdisciplinary Applied Mathematics*. Springer; 1998.

How to cite this article: Pfefferkorn R, Betsch P. Hourglassing- and locking-free mesh distortion insensitive Petrov–Galerkin EAS element for large deformation solid mechanics. *Int J Numer Methods Eng*. 2022;1-37. doi: 10.1002/nme.7166

APPENDIX A. HIGHER ORDER INCOMPATIBLE MODES

In this appendix we cover analytic solutions for higher order displacement modes in isotropic linear elasticity. These solutions inspire the modified higher order enhanced modes employed in Sections 3.2.3 and 3.2.4. The benefit of these modes is that they allow to circumvent the tedious orthogonalization required for the element by Pfefferkorn and Betsch.[18] Nadler and Rubin[45] propose a set of higher order displacement modes and use it to design their Cosserat point element. Here we consider similar displacement modes of the form

$$\mathbf{u} = \begin{bmatrix} xyz \\ 0 \\ 0 \end{bmatrix} + \frac{\nu}{6} \begin{bmatrix} 0 \\ -3y^2z + z^3 \\ -3yz^2 + y^3 \end{bmatrix}, \tag{A1}$$

where $\mathbf{x} = [x, y, z]^{\mathrm{T}}$ are physical coordinates and ν is the Poisson's ratio. The standard relations yield the corresponding strain and stress field given by

$$\boldsymbol{\varepsilon} = \frac{1}{2} \begin{bmatrix} 2yz & xz & xy \\ xz & 0 & 0 \\ xy & 0 & 0 \end{bmatrix} - \nu \begin{bmatrix} 0 & 0 & 0 \\ 0 & yz & 0 \\ 0 & 0 & yz \end{bmatrix}, \qquad \boldsymbol{\sigma} = \mu \begin{bmatrix} 2yz(\nu+1) & xz & xy \\ xz & 0 & 0 \\ xy & 0 & 0 \end{bmatrix}, \tag{A2}$$

which have a particularly simple form in comparison to the modes proposed by Nadler and Rubin.[45] Since the ansatz for the displacement already contains the trilinear term xyz (see Section 3.2.2), only the second part of (A1) has to be added in the sense of incompatible modes. Thus, the enhanced field of the higher order enhanced modes should have the form of the second matrix in (A2) which inspired the fields in (34) and (37). Figure A1 shows the respective parts of the displacement field given in (A1). Unfortunately, (A1) cannot directly be transferred to the skew coordinate frame in case of distorted meshes. However, it seems that using (34) and (36) yields good results even in distorted meshes, that is, when the skew frame is not orthogonal.

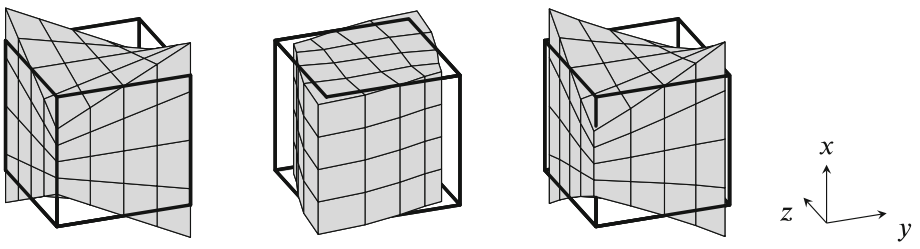

FIGURE A1 Trilinear (left), enhanced (middle), and total (right) displacement field (A1) scaled with 0.5, 2.0, and 0.5, respectively. Computed with $\nu = 0.3$ for a block $\mathcal{B}_0 = [-1, +1]^3$ (thick black line).